Estimation of Water Cloud Properties from Satellite Microwave, Infrared and Visible Measurements in Oceanic Environments. II: Results

Bing Lin[1], Patrick Minnis[2], Bruce Wielicki[2], David R. Doelling[3], Rabindra Palikonda[3], David F. Young[2], and Taneil Uttal[4]

[1]Hampton University, Hampton, VA 23668
[2]NASA Langley Research Center, Hampton, VA 23681-0001
[3]Analytical Services and Materials, Inc., Hampton, VA 23681
[4]NOAA Environmental Technology Laboratory, Boulder, CO 80303

Submitted to J. Geophys. Res.
Revised in September 1997

ABSTRACT

A microwave MW method for deriving cloud liquid water path *LWP* and cloud water or center temperature *Tw* is validated using soundings and results from a visible VIS and infrared IR retrieval method. The two retrieval methods are combined into a single technique, MVI, to estimate the frequency of multi-layered clouds and the effective droplet radius r_e in single-layered clouds. These techniques were applied to Meteosat and Special Sensor Microwave Imager (SSM/I) data taken during June 1-28, 1992 over the Atlantic Stratocumulus Transition Experiment (ASTEX) region. For low-clouds, as identified with the VIS-IR method, *Tw* on average is nearly the same as the VIS-IR cloud-top temperatures *Tc*. For mid-level clouds, *Tw* is about 8 K warmer than *Tc* because of either large cloud thicknesses or multi-layered clouds. When high clouds are found by the VIS-IR method, *Tc* is ~30 K colder than *Tw* indicating that lower level liquid water clouds may be detected by the MW method.

Except for overcast high clouds, the means and standard deviations of *LWP* derived from MW and VIS data are very similar if r_e is assumed to be 10 μm. The greatest difference is found for mid-level clouds. The modes of the MW *LWP* retrievals for low and middle clouds are about 0.05 and 0.10 kg/m^2, respectively, values that are ~0.05 kg/m^2 smaller than the corresponding means. A negative correlation between *LWP* and *Tw* was found for low clouds. The mean *LWP* for all cloudy cases (broken and mixed low and mid-level) is ~0.08 kg/m^2. The mean MW *LWP* derived for overcast high clouds is approximately half that for low clouds. Based on the matched *Tw* and *Tc* obsevations, the estimated frequencies of multi-layered high, middle and low clouds are about 36%, 19% and 0%, respectively, values that are similar to cloud radar measurements. Matched satellite and ground-based radar data show that the MVI technique can separate cloud layers when high ice clouds overlap lower liquid water clouds. The distributions of r_e for water clouds are about the same for low, middle and broken clouds with mean and standard deviations of ~12 and 10 μm, respectively. The medians are ~10 μm, while the mode r_e values are considerably smaller. The frequency of large droplets (r_e > 16 μm) suggests that drizzle occurs in ~30% of the matched Meteosat-SSM/I cloudy conditions.

1. Introduction

Clouds affect both atmospheric hydrological and energy cycles. They release latent heat into the atmosphere and transport fresh water among oceanic basins affecting sea surface salinity, ocean circulation, and, ultimately, climate. Clouds have both macro- and microstructures, including horizontal and vertical variations in liquid/ice water path (*LWP*/*IWP*), optical thickness, temperature, height, fractional coverage, and particle size, shape, and phase. All of these properties are critical for determining atmospheric radiation fields [*Wielicki et al*. 1995] necessitating the development of reliable monitoring methods.

Among many satellite cloud remote sensing problems, two are especially considered in this study: multi-layered clouds and cloud water droplet size. Multi-layered clouds, together with changes in cloud particle size and phase (water or ice), determine both cloud radiation and cloud feedback for changing climate [*Twomey* 1977; *Gupta et al*. 1992; *Charlock et al*. 1994; *Wielicki et al*. 1995]. Surface climatological observations show that about 40-50% of the clouds are multi-layered [*Poore et al*. 1995; *Hahn et al*. 1982, 1984; *Warren et al*. 1985; *Warren et al*. 1988; *Tian and Curry* 1989]. Satellite observations of multi-layered clouds, at present, are limited to cases of thin cirrus over stratus [*Baum et al*. 1994].

Using satellite visible (VIS) and infrared (IR) radiance data, *Han et al.* [1994] and *Luo et al.* [1994] found that warm clouds usually have relatively narrow distributions of effective particle radii with mode and mean values about 10 μm. Although generally agreeing with these satellite estimates, in situ observations often produce wider particle size spectrums [*Heymsfield* 1993 and references therein] and even larger drizzle droplets [*Minnis et al.* 1992; *Gerber* 1996 and references therein]. This difference reflects that the satellite VIS and IR observations are usually sensitive to thin clouds or the top portion of thick clouds [*Nakajima and King* 1990; *Nakajima et al.* 1991], making it difficult to detect the particles in the lower portions of optically thick clouds or larger drizzle particles below [*Han et al.* 1994]. Thus, new methods are needed to estimate the properties of thick and/or multi-layered clouds.

In Part I [*Lin et al.* 1997], we simulated Special Sensor Microwave/Imager (SSM/I) brightness temperatures at the top of the atmosphere for non-precipitating clouds and proposed to estimate cloud water temperature Tw and LWP using VIS, IR and microwave (MW) satellite observations. Because non-precipitating ice clouds do not significantly scatter and absorb microwave radiation, MW remote sensing methods usually cannot detect non-precipitating ice clouds [*Lin et al.* 1997]. Thus, by combining IR and MW methods, it should be possible to detect thick non-precipitating ice clouds at the top by a VIS-IR technique and liquid water clouds below by MW methods, i.e., we can detect multi-layered clouds, especially when both layers are thick. It was shown in Part I that a method using SSM/I 37- and 85-GHz radiances together could retrieve LWP and Tw simultaneously. Although theoretically Tw can only be derived to within $\pm$ 1 - 2 km for clouds with LWP < 0.5 mm (nonprecipitating clouds) with this approach, the technique represents an improvement over other methods that assume a fixed value of Tw relative to the sea surface temperature SST, especially in areas where the potential range in liquid-water cloud temperature is greater than ~25°C.

The effective particle radius of non-precipitating water clouds may be estimated by using cloud optical thickness derived from reflected sunlight and microwave LWP [*Minnis et al.* 1992; *Young et al.* 1992; *Zuidema and Hartmann* 1995; *Greenwald et al.* 1995]. Because the LWP values from microwave methods are not sensitive to the size of cloud water particles as long as the particles are relatively small (< about 150 μm) and represent column liquid water amount, the effective particle radii reflect the column-averaged values, not just the top portion of clouds.

Because non-precipitating clouds are the dominant cloud type in determining the atmospheric radiative energy budget [*Lin and Rossow* 1996; *Wielicki et al.* 1995], we do not consider precipitating clouds in this study. Satellite-observed data used here are discussed in section 2. Section 3 describes our cloud liquid water path and temperature retrieval scheme based on microwave radiative transfer model simulated lookup table for SSM/I brightness temperatures. The following section discusses the differences between the IR- and MW-observed cloud temperatures, analyzes the observed LWP and particle size values, and investigates multi-layered clouds. Finally, we summarize conclusions in section 5.

2. Datasets

This study uses visible (~0.65 μm), infrared (~11 μm), and microwave satellite measurements taken June 1-28, 1992 over the North Atlantic (25° - 40° N, 330° - 345° E) during the Atlantic Stratocumulus Transition Experiment (ASTEX). The VIS-IR data come from Meteosat located at 0° longitude and are used to detect cloudy and clear sky areas, measure sea surface temperature, cloud-top temperature, cloud amount, and cloud optical thickness (or cloud liquid water path) using the hybrid bispectral threshold method (HBTM) [*Minnis et al.* 1987]. The true bandwidth for the Meteosat VIS channel is 0.4 - 1.1 μm; however, it has been calibrated against channel 1 of the NOAA-11 Advanced Very High Resolution Radiometer (AVHRR) and is considered to be equivalent to the narrower AVHRR channel over ocean areas. The data were taken half hourly at a 5-km resolution and analyzed on a 0.5° latitude/longitude grid. Because liquid water clouds are the focus, this analysis only derives cloud optical thickness τ for water clouds (i.e., for low and middle level clouds) assuming cloud water particles are spherical with an effective droplet radius, r_e = 10 μm. Because reflected visible radiances are not very sensitive to r_e for a given τ, the uncertainties in estimated optical

thicknesses associated with errors in the r_e are generally small [*Han et al.* 1994].

The MW data were measured with the Defense Meteorological Satellite Program (DMSP) SSM/I on the DMSP F-11 satellite. DMSP F-11 passed over the ASTEX region twice per day near 0630 and 1830 UTC. The SSM/I is a seven-channel, passive thermal microwave radiometer. It measures radiances at frequencies of 19.35, 22.235, 37.0 and 85.5 GHz (hereafter referred to as 19, 22, 37 and 85 GHz for short). Vertical (v) and horizontal (h) polarization measurements are taken at all frequencies, except at 22 GHz where SSM/I only has a vertically polarized channel. The viewing zenith angle of SSM/I at Earth's surface is nearly constant at ~53°. The spatial resolution of SSM/I observations depend on frequency. For the frequencies used to estimate *LWP* and *Tw*, the resolution changes from ~13 km at 85 GHz to ~40 km at 37 GHz. The microwave antenna temperatures from the F-11 SSM/I were converted to brightness temperatures with a method provided by Wentz [1988]. The SSM/I data are used to estimate near-sea-surface wind speed *WS*, column water vapor *CWV*, *LWP* and *Tw*. The uncertainties in the parameters were discussed in Part I [*Lin et al.* 1997]. The precipitating and non-precipitating clouds are separated by the polarization difference of 37-GHz brightness temperature *Tb* with a threshold of 37K [*Lin and Rossow* 1994 and 1997; *Goodberlet et al.* 1990]. To combine the Meteosat and SSM/I datasets, we collocate the SSM/I and Meteosat data taken within $\pm$ 15 minutes into 0.5° latitude-longitude boxes.

The results are compared with ground-based *LWP*, radiosonde, and cloud radar measurements made during ASTEX experiment to verify the *LWP*, cloud height, and cloud layering estimated from the satellite data.

3. Retrieval Scheme

For simplicity, the retrieval scheme is designated the microwave-visible-infrared or MVI method. The determination of *LWP* and *Tw* using MW data is based on MW radiative transfer model (MWRTM) simulations. According to the simulated results, brightness temperatures at 37 and 85 GHz, especially Tb_{37h} and Tb_{85v}, are sensitive to both cloud water amount and temperature, but their variations with *LWP* and *Tw* differ significantly. *Tb* at 37 GHz rises with increasing *LWP* and/or decreasing *Tw*, while Tb_{85} decreases with decreasing *Tw* and its variation on *LWP* depends on the upwelling MW radiation below the clouds and on *Tw*. These *Tb* differences at 37 and 85 GHz make it possible to estimate *LWP* and *Tw* simultaneously using SSM/I data. The details of the MWRTM and simulated results are given in *Lin et al.* [1997].

A lookup table for SSM/I brightness temperatures was produced using the results of MWRTM computations that simulate weather conditions ranging from clear to non-precipitating cloudy sky cases. The relative calibration between the simulated results and SSM/I observations was made using clear-sky cases [*Lin et al.* 1997]. The biases between the observed and simulated brightness temperatures in cloudy skies are assumed to be the same as clear-sky ones. We should emphasize that the current calibration is a relative one and its results may not be applicable to other datasets.

In addition to atmospheric profiles of temperature and humidity, trace gas content and oceanic conditions, there are five basic geophysical parameters within the lookup table: *SST*, *WS*, *CWV*, *LWP*, and *Tw*. Simulated brightness temperatures within the table account for *SST* from -1 to 33° C; *WS* from 0 to 40 m/s; *CWV* 5 -100 kg/m^2; *LWP* 0 -- 1.0 kg/m^2 and *Tw* from *SST* to -40° C. The first three parameters, together with the SSM/I-observed brightness temperatures, are used as input for the MW retrieval method. The last two quantities are derived from the data. Near sea-surface wind speeds are MW retrievals based on the method of *Goodberlet et al.* [1990], while water vapor is estimated from the *Schluessel and Emery* [1990] scheme (hereafter referred to as the SE scheme). To reduce *CWV* uncertainties, averaged values of four neighboring SSM/I pixels are used as input to estimate *LWP* and *Tw* [*Lin et al.* 1997]. During the retrieval of *LWP* and *Tw*, the small *CWV* bias between the model estimates and the SE scheme is corrected using the SSM/I *Tb* relative calibration [*Lin et al.* 1997]. The exact error source producing the *CWV* bias is unknown. It may be introduced by the bias errors of the SE scheme or by biases in the SSM/I brightness temperature at 22 GHz.

To estimate *LWP* and *Tw*, we first use the HBTM-estimated cloud-top temperature *Tc* for the coldest clouds in each matched grid box to select a value of *Tw* from the lookup table of simulated SSM/I *Tbs*. The selected temperature,

the nearest lookup table value colder than the HBTM result, is used as the first guess of Tw. If Tc is colder than -40° C, the first guess is set to -40° C (note: when HBTM cloud fraction is zero, $SST - 8K$ is chosen as the first guess of cloud water temperature). In the second step, we initially estimate LWP by comparing the SSM/I-observed Tb_{37h} with the values in the lookup table corresponding to the guessed Tw and input SST, WS, and CWV values. The lookup table is then used to estimate Tb_{85v} based on the initial estimates of LWP and Tw. This temperature is compared to the observed SSM/I value. If the differences between the observed and estimated values of Tb_{85v} reach a minimum, the retrieval process is finished and gives all initial estimates as final outputs. Otherwise, the cloud water temperature is increased (cloud height is decreased), and the second and third steps are repeated until the consistency requirements are satisfied.

This method automatically searches for the best water-cloud solutions by proceeding from high to low altitudes without interference from ice clouds. Even if the coldest clouds found by HBTM are ice clouds, the current retrieval scheme ignores them and estimates LWP and Tw of any lower-level clouds, even if the ice clouds are thick.

In the MVI technique, the effective particle radii for water clouds are estimated from the LWPs of the VIS and MW methods. Because VIS-estimated cloud optical thickness is not very sensitive to cloud effective droplet size [*Han et al*. 1994] and LWP is proportional to cloud effective droplet radius [*Stephens*, 1984; *Lin and Rossow*, 1994], we can estimate the effective droplet radius for a given set of matched measurements as:

$$r_e = r_{ea}\,, \qquad (1)$$

where r_{ea} is the effective droplet radius (10 μm) used by the HBTM to retrieve cloud optical thickness. LWP_{MW} is the cloud liquid water path obtained from the current SSM/I retrieval scheme. LWP_{VIS} is the LWP value estimated from the VIS optical thickness and r_{ea} [*Lin and Rossow* 1994]. The relationship in equation (1) can be used to estimate the droplet sizes in water clouds and to evaluate the consistency between the observed r_e and r_{ea} as discussed later. This approach has been applied using various combinations of MW and reflected solar radiation data and yields values of r_e that compare well with in situ data (e.g., Minnis et al. [1992]).

4. Results and discussion

a. Cloud temperatures

In the ASTEX region, persistent maritime stratocumulus clouds dominate the exchange of atmospheric radiation. These clouds are low (< 2 km). Some middle (2 to 6 km) and high (> 6 km) clouds associated with frontal systems also occur in the region. Based on the cloud amounts from HBTM method, the estimates for both VIS/IR and MW methods are separated into four groups: cases with low, middle, and high overcast and total-cloud samples (or all cloudy atmospheres, includes broken and overcast clouds). The low, middle, and high overcast cases constitute about 17.4, 3.1, 0.8% of the total number of samples, respectively.

For low-cloud overcast cases, Tw is strongly and positively correlated with Tc. Figure 1a is a scatterplot of Tw and Tc for 500 randomly sampled low-cloud pixels. The root-mean-square differences are ~3K, a value within the theoretical uncertainty of the MW retrieval. Although there is considerable scatter between Tw and Tc and the temperature range is limited, the correlation coefficient (R = 0.62) between them is significant at the 99% confidence level. When averaged in 1-K intervals of Tc for all data, Tw varies almost linearly with Tc and has a linear correlation coefficient of 0.99 (Figure 1b) with minimal differences between the mean bin values.

Midlevel clouds show a different level of correlation. In Figure 1c, part of the data fall around the line of agreement while a larger portion, concentrated near Tw = 286 K, shows no apparent correlation. The resulting value of R is 0.41, less than the low-cloud value, but still significant as indicated by the slope in the bin-averaged data in Figure 1d. Without the data along the line, the correlation would be minimal. The bifurcation in the scatterplot can be explained by two sets of conditions that would yield midlevel clouds in the HBTM analysis. When thin clouds overlay thicker low clouds, the data can be interpreted as midlevel clouds although the bulk of the liquid water is confined to the low clouds. Clouds above 6 km must be optically thick ($\tau > 4$) before they can be interpreted as high clouds. The spread of Tc between 280 and 260K at Tw = 286K likely corresponds to upper-level clouds at various altitudes and optical

depths overlying the low clouds at ~286K. Data along the line of agreement are probably due to the occurrence of colder water clouds with no significant cloudiness below. There is little correlation between *Tc* for the HBTM overcast high clouds and the corresponding values of *Tw* (not shown). The high clouds are most likely composed entirely of ice and, therefore, should have no general relationship to the temperature of any underlying liquid water clouds.

Figures 1e and 1f show the raw and bin-averaged scatterplots, respectively, for the total cloud category. Although much of the data are similar to the overcast low-cloud results in Figure 1a, the correlation falls between the low and mid-level results with $R = 0.51$ and 0.96 for the raw and bin-averaged data, respectively. Excellent agreement between *Tc* and *Tw* can be seen for $Tc > 288$K in Figure 1e. The values of *Tw* for $Tc < 285$K appear to branch into two areas as in Figure 1c for the midlevel clouds. Here, however, there appears to be some slope in the scatter of points above the line of agreement. Some points below the line of agreement deviate more than seen in the previous plots probably because of the occurrence of some partially cloud-filled SSM/I pixels. The agreement seen for the low clouds is more evident in Figure 1f for $Tc > 285$K. At colder temperatures, the bin-averaged values are above the line of agreement as seen for the midlevel clouds, but the deviations are considerably smaller, possibly because of a reduced fraction of mid- or thin high-level clouds over the low clouds. In those instances, the average value of *Tc* will be greater than that for the overcast midlevel cloud cases. Overall, the high levels of correlation exhibited in Figure 1 demonstrate that the two methods are generally measuring similar cloud properties when the liquid water clouds are unobscured and that the MW technique can measure changes in low-cloud temperature even when higher ice clouds hide the low clouds from the IR sensor.

Figure 2 shows the histograms of *Tc* and *Tw* for all four categories. For low clouds (Figures 2a and b), both methods give a mean cloud temperature ~285K with a standard deviation of ~3K, indicating the heights of marine stratocumulus clouds are rather stable, generally near 1 ± 0.5 km based on the mean *SST* of approximately 290 K. The statistical distributions of the cloud temperatures are more or less Gaussian shaped although the *Tc* distribution is slightly narrower than that of *Tw*. These differences between the MW- and IR-estimated cloud temperatures (Figure 3) can be explained by uncertainties in the *Tw* and differences in the definitions of cloud temperature (cf. Figure 1 and *Lin et al*. [1997]). The mean difference between the MW and IR low-cloud temperatures (Figure 3a) is approximately 0.3 K with a standard deviation ~3K. The latter value is almost the same as the theoretical uncertainties in *Tw* [*Lin et al*. 1997]. The IR temperature corresponds to some temperature just below cloud top, within 25 -100 m depending on the cloud particle concentration and cloud thickness, while the MW temperature corresponds to a column-averaged value of cloud liquid water temperature, usually a location slightly above the center of the cloud in a single layer system. As the optical depth decreases, the value of *Tc* increases toward values lower in the cloud or even to some value between the *SST* and the cloud base temperature when $\tau < 4$. For thick clouds, however, *Tw* should, on average, be greater than *Tc*. The majority of clouds, as measured by the NOAA/WPL 8-mm radar on Porto Santo Island (33.04° N, 343.80° E), were less than 300-m thick [*Uttal and Frisch, 1994*]. If it is assumed that the average low-cloud thickness is 200 m, *Tw* corresponds to the cloud center, and *Tc* represents the temperature at 50 m below cloud top, then a difference of only 50 m would separate the altitudes corresponding to the derived temperatures. Thus, for -7.1°C/km lapse rate in the marine boundary layer (e.g., Minnis et al. [1992]), *Tw* should be ~0.35K warmer than *Tc*, for the low-cloud cases, consistent with the observed mean difference.

Overcast mid-level clouds show some significant differences in *Tc* and *Tw* (Figures 2c and d) as expected from Figure 1c. The MW cloud liquid water temperatures are about 8K warmer, on average, than the IR-estimated cloud-top temperatures (*Tc* ~275 K), although the standard deviations (~5 K) and shapes of the frequency distribution are similar. In addition to the occurrence of thin high or mid-level clouds over denser low clouds noted earlier, this difference may reflect the capability of MW methods to penetrate water clouds much deeper than IR methods. The MW cloud temperature is a column-averaged value of cloud liquid water temperature, not the temperature near cloud top derived with the IR technique. The peak frequencies of *Tw* for middle clouds (Figure 2d) are located near those for low clouds (Figure 2b) suggesting that most of the liquid water is

confined in the lower levels of the cloud. The cold tails in both MW and IR cloud temperature distributions probably result from clouds that are 4 to 6 km high. The small frequency of colder clouds in the MW histogram relative to the IR histogram suggests that the occurrence of thin layers of high or midlevel clouds over thicker low clouds is relatively common for the scenes classified as overcast midlevel by the HBTM.

The cloud temperature differences between the MW and IR methods (Figure 3b), unlike low-cloud cases, have a strong statistical peak at ~8 K and vary from -4 to 20 K. This difference, considerably larger than the MW biases for moderately thick clouds, suggests that most middle clouds are below 4 km and are either multi-layered or about 1.5-km thick, conditions similar to the ground observations of *Wang and Rossow* [1995] and *Poore et al*. [1995]. The negative differences are probably due to the noise in the retrieval method (cf. *Lin et al.* [1997])

The MW and IR high-cloud temperature distributions (Figures 2e and f, respectively) are significantly different. By definition, *Tc* is very cold, ranging from 250 to 220 K with mode values near 240 K. In contrast, *Tw* can be as warm as *SST* or as cold as -40°C (the lower temperature limit for supercooled liquid water) with a mode of 286 K (Note that in many high cloud overcast cases, near zero *LWP* values are found because of single-layered ice clouds (see later and cf. Fig. 7g), thus *Tw* may represent surface temperature, instead of cloud water temperature.). The mean IR cloud-top temperature is ~238 K with a 7-K standard deviation. The corresponding mean and standard deviation for *Tw* are ~270 K and 20 K, respectively. The large standard deviation in *Tw* is due to the wide variation in cloud liquid water height below the high clouds or to the dramatic temperature contrast between cloud top and sea surface for single-layered ice clouds. Most values of *Tw* corresponding to the HBTM-derived high clouds are equal to or slightly warmer than the *SST*. In these cases, the high clouds are probably composed entirely of ice particles. The clouds with $Tw < SST$ may represent multi-layered cases. From this figure, it seems that the lower-level clouds ($Tw < 280$K) may be more or less randomly distributed between about the -40°C level and the surface. Some of the extremely cold liquid-water clouds ($Tw < 250$K) in Figure 2f may be due to the uncertainties in the temperature retrieval discussed by *Lin et al.* [1997]. The apparent random distribution of lower-level clouds for temperatures less than the modal value, is consistent with that of *Tian and Curry* [1989] and is also apparent in the differences between *Tc* and *Tw* (Figure 3c). These temperature differences vary from -5 to 68 K and are rather uniformly distributed, especially between 0 and 40 K. As noted for the midlevel clouds, the negative differences reflect the random uncertainty in the MW retrieval for the thinner single-layered, cold liquid water clouds. The wider distribution of *Tw* relative to the low and midlevel cases is probably due to the occurrence of cirrus over both stratus and higher liquid water clouds associated with frontal systems. The appearance of optically thick high clouds is indicative of disturbed conditions that may alter the usual vertical structure in the stratocumulus region.

Figures 2g and 2h compare the frequencies of *Tc* and *Tw* for all cloudy cases. The basic features of the two kinds of cloud temperatures are the same: mostly warm (mean temperatures are about 284 K) and moderately variable (standard deviation is about 7 K, a value between that for the high and low clouds). The long cold tails in both histograms represent increasing amounts of middle and high clouds as suggested in Figure 1f. The larger positive temperature differences between the MW and IR methods (Figure 3d) are most likely due to the presence of middle and high ice clouds.

If all four groups of *Tw* values in Figure 2 are considered, one obvious feature is that the mode values are about 285 K. This indicates not only that marine stratocumulus clouds are the dominant cloud type in the ASTEX region, but also that the heights of the stratocumulus clouds are more or less uniform whether higher clouds are present or not. This feature is not evident when values of *Tc* are considered because the IR data do not reveal the clouds underneath the upper layer decks.

Figures 1-3 show that there are large differences between *Tc* and *Tw* for overcast middle and high clouds. In order to further confirm these features, we examine the divergent effect of high over low clouds on the correlation between *Tc* and *Tw* using cloud layers estimated from radiosonde data. During ASTEX, radiosondes were nominally launched every 3 hours from Santa Maria (37.0°N, 334.8°W) and Porto Santo Islands [*Syrett*, 1993]. Each of these soundings was analyzed to determine the number of cloud layers, the center and top

temperatures for each layer, the average center temperature for all of the layers, and the mean center temperature of all of the layers below the highest layer. The means were computed as the thickness-weighted average temperatures. A cloud layer consists of all contiguous measurements having a dewpoint depression that is less than or equal to 1K. To a first approximation, the temperature of the highest layer is equivalent to *Tc*. For multilayer systems with ice clouds (*Tc* < 270K) at the top, it is assumed that the mean temperature of all of the lower layers is equivalent to *Tw*. If it is assumed that all of the cloud layers are liquid water, then their mean center temperature is equivalent to *Tw*.

Figure 4 shows the scatterplots for these two cases. In Figure 4a, where it is assumed that all layers are liquid water, some of the data fall along the agreement line with many points above the line. The center temperature is greater overall than the cloud-top temperature with the difference increasing as *Tc* decreases. The correlation is strong with $R = 0.88$. If the colder clouds are assumed to be ice clouds that would not be included in the liquid-cloud center average, the scatterplot (Figure 4b) shows the bifurcation seen in Figure 1c. The few data that fall near the line for *Tc* < 270K in Figure 4b correspond to single layer clouds or to those with only a very thin low cloud. The remaining cold clouds have values of *Tw* that straddle 285K, similar to the pattern in Figure 1c. For this scatterplot, $R = 0.44$, a value close to that found in the middle cloud case. Although the data taken from these islands do not necessarily represent all of the ASTEX domain and it is difficult to detect high thin cirrus using the radiosonde approach, it is encouraging that the soundings can explain much of the gross variation in the correspondence between the two cloud temperatures. Smaller variations about the line of agreement are due to noise in the data and in the technique discussed by *Lin et al.* [1997]. The results in Figure 4 also clearly show that the low stratocumulus layers persist even in disturbed multilayered cloud conditions confirming the conclusions deduced from the results in Figures 1, 2 and 3. The similarities between the radiosonde and satellite cloud correlations and the correspondence between *Tc* and *Tw* in Figure 1 show the combined MW approach provides a good estimate of cloud center temperature for liquid-water clouds even when ice clouds overlay the lower clouds.

b. LWP comparisons

One means to evaluate the current *LWP* retrieval scheme is to compare it with other techniques such as that of *Greenwald et al.* [1993]. Their method estimates *LWP* and *CWV* simultaneously from SSM/I data using a simplified physically based microwave method. *Greenwald et al.* [1993] choose *Tw = SST-6K*, a value typical of low-level marine clouds. The value of *Tw* significantly affects *LWP* estimates [*Lin and Rossow* 1994; *Lin et al.* 1997]. Therefore, it is impractical to compare the current retrieval method with their method for scenes affected by middle and/or high clouds. Thus, we only consider low-cloud cases here. Figure 5 shows the results for overcast low clouds during ASTEX. In these cases, *LWP*'s estimated from the two methods are almost the same with average differences ~0.006 kg/m^2. Both methods use the same sea surface temperatures, near-sea-surface wind speed, and the SSM/I 37-GHz brightness temperature as inputs to estimate *LWP*. The cloud liquid water temperatures from the current MW method are similar to the IR observations, as just discussed, i.e., the water temperature differences between our estimates and *SST-6K* are small. Thus, the excellent agreement between the two methods is not surprising.

Ground-based passive microwave measurements were taken during ASTEX from Porto Santo Island with a 30-second temporal sampling rate [*Snider et al.*, 1996] and from the island of Santa Maria [*Albrecht*, 1996]. To compare microwave satellite observations with the Porto Santo ground data, all SSM/I observations were analyzed for the region between 32.5 and 33.5° N and between 15.7° to 16.7°W, but not containing Porto Santo Island itself. Because of the fundamental spatial differences between satellite and ground-based observations and large spatial and temporal variations of cloud liquid water fields, the SSM/I observations are compared with the temporally averaged values of the surface-based *LWP* measurements. Figure 6 compares the SSM/I retrievals with ground-based 1-hour *LWP* means for overcast cases. Generally, the satellite *LWP* estimates agree with ground-based *LWP* data. The mean difference between the ground-based and SSM/I *LWP* estimates is 0.034 kg/m^2 or about 30% of the mean value. The largest differences occur when the ground instrument locally observes relatively high (> 0.2 kg/m^2)

LWP values. For these two estimates of LWP, R = 0.54, significant above the 99% confidence level. The major differences between the two observations can be explained by spatial and/or temporal differences in cloud liquid water path, as indicated by multiple values of LWP_{MW} for a single ground-based LWP observation in the figure. The spatial variability around the islands will be greater than that typically found over the ASTEX domain because of island effects. The local effects of island may also cause a bias in the cloud properties over the island relative to the surrounding ocean. The mean LWP from the Santa Maria microwave radiometer is about 0.1 kgm^{-2} for the ASTEX period compared to a mean LWP_{MW} of 0.104 kgm^{-2} indicating excellent agreement for two different portions of the domain.

c. LWP estimates

Cloud liquid water path is one of the cloud macrophysical factors affecting cloud thickness and radiation. The visible-channel liquid water path LWP_{VIS} is obtained from the VIS optical depth as in *Minnis et al*. [1992] assuming that r_{ea} is 10 μm. This droplet radius may over- or underestimate LWP depending on the true effective particle radius of the observed clouds. The LWP_{MW} values, on the other hand, are generally independent of cloud droplet size [*Lin et al*. 1997 and references therein]. Thus, the LWP_{VIS} and LWP_{MW} retrievals can be seen as independent observational values. Correlation between these two quantities yielded R = 0.48, 0.44, and 0.63 for low, middle, and all clouds, respectively. These values are significant above the 99% confidence level.

The correspondence between the two liquid water paths can also be examined using the frequency distributions shown in Figure 7 for the four cloud categories. Because the cloud particles in high clouds are generally ice, no LWP values are retrieved from the HBTM method. Thus, for overcast high clouds (Figure 7g), we only consider LWP_{MW} estimates. In low-cloud overcast cases (Figures 7a and b), the means (~ 0.1 kg/m^2) and standard deviations (~ 0.08 kg/m^2) for both datasets are almost the same because both methods estimate column water amount and the averaged effective particle radius is about 12 μm (see later), a value close to r_{ea}. The general distributions of the two types of LWP are similar although the LWP_{MW} distribution is broader than that for LWP_{VIS}. This difference in width is due to a combination of uncertainties in the MW and VIS retrievals and to the use of a single droplet size in the HBTM retrieval. Variable droplet radii would increase the number of possible values for LWP_{VIS} for a given reflectance. Both distributions have mode values near 0.04 kg/m^2 and a long tail toward LWP as large as 0.4 kg/m^2, near the upper limit of non-precipitating clouds [*Lin and Rossow* 1994; *Greenwald et al*. 1993]. A small portion (about 5%) of the LWP_{MW} data are less than zero possibly due to errors in *CWV*, *WS* and *SST* or the SSM/I noise, as discussed earlier.

In overcast middle cloud cases (Figures 7c and d), the means (~ 0.14 kg/m^2) and standard deviations (~ 0.1 kg/m^2) for both LWP_{VIS} and LWP_{MW} are also very similar. The mean midlevel values of LWP are greater than their low-cloud counterparts by about 30 - 40%. Using the cloud thicknesses derived from the island radiosonde data and assuming that low clouds correspond to $Tc \geq$ 281K, it was found that the HBTM midlevel clouds should be ~ 30% thicker than the midlevel clouds. If this result is representative of the ASTEX domain, then the liquid water content (LWC) values for middle level clouds should be almost the same as those in low clouds. The mode value for midlevel LWP_{VIS} is similar to that of low clouds, while the LWP_{MW} mode (~ 0.1 - 0.15 kg/m^2) is considerably larger . This discrepancy may result from the differences in the spatial resolutions of VIS and MW instruments, from differences in the droplet sizes, or from contamination of the VIS reflectance by ice clouds.

To compare the liquid water paths for all cloudy atmospheres, the cloud fraction must be taken into account by multiplying LWP_{VIS} by the HBTM cloud fraction. The LWP mode values for the cloudy atmospheres (Figures 7e and f) are between 0 and 0.05 kg/m^2. Their means are significantly less than those for low and middle overcast clouds, consistent with the classification of thinner, broken clouds. The clear portion of the scene would diminish the cloud influence on the MW radiance reducing the scene LWP_{MW} compared to a scene overcast with the same clouds. Cloud frequency of occurrence also decreases with increasing cloud thickness (i.e., most observed clouds are thin and low) so most of the observations fall into the total cloud category. Similar features have been found in other satellite MW studies [*Lin and*

Rossow 1994 and 1996; *Greenwald et al*. 1993 and 1995; *Liu and Curry* 1993]. Nevertheless, these clouds are very important because they have a significant impact on shortwave radiation and will affect the surface flux of longwave radiation [e.g., *Wielicki et al*. 1995].

The *LWP* values for high-cloud overcast cases (Figure 7g) are slightly smaller than those for the broken or all cloud category. The mode value of LWP_{MW} is the same as or slightly smaller than that for the low clouds but has a greater frequency. The more frequent occurrence of low *LWP* is probably due to thin cold clouds superimposed on the distribution of low-cloud LWP_{MW} underneath the cirrus. Small LWP values were also found for cold clouds by *Lin and Rossow* [1994 and 1996]. The near-zero and negative values of that have Tw close to *SST* are probably indicative of conditions that are essentially free of cloud liquid water. Pixels having those characteristics should probably have both Tw and LWP_{MW} set to zero. The positive LWP_{MW} values, especially those significantly larger than the LWP_{MW} uncertainties, probably correspond to low-level liquid-water clouds below the ice clouds.

The liquid water content of these clouds can be estimated using radar determinations of cloud thickness. *Uttal and Frisch* [1994] and *Albrecht* [1996] derived cloud thickness over Porto Santo and Santa Maria, respectively. Their results for clouds below 4 km yield thicknesses that vary from 200 m over Santa Maria to 360 m over Porto Santo. The average value of LWP_{MW} around Porto Santo is 0.115 kg/m^2. Dividing the near-island average values of LWP_{MW} by the mean radar thicknesses yields an average *LWC* between 0.3 and 0.5 g/m^3. These values are within the range of the in situ observed ASTEX *LWC* taken near the cloud middle [e.g., *Gerber* 1996].

d. Multilayered clouds

Multilayered clouds are identified as those cloudy MW pixels that have significant differences between the IR and MW cloud temperatures. The HBTM can identify different cloud layers but not whether the layers are overlapped. The MW retrieval provides only one temperature for each 35-km pixel providing no information about partial coverage by different layers of clouds. Therefore, we will not consider multilayer broken clouds any further here. To take into account the advantages of each technique, we will examine the multilayer cloudiness only for those pixels classified as overcast in a single layer by the HBTM. Figure 8 shows contours of the relative frequencies of LWP_{MW} and $\delta Tc = Tw - Tc$ for the three overcast groups. For low-cloud overcast cases (Figure 8a), all observations are concentrated near δTc = 0K, indicating no cloud overlap. For midlevel clouds (Figure 8b), some observations have temperature differences as great as 20 K with considerable cloud liquid water amounts (> 0.04 kg/m^2). Many high-cloud *LWP* values (Figure 8c) are near zero over the full range of temperature difference, indicating only ice clouds in the region as suggested earlier. Other clouds have large temperature differences (> 15 K) and significant amounts of cloud liquid water. These features most likely indicate the presence of lower level clouds underneath the layer viewed by Meteosat.

To quantitatively obtain the frequencies of multilayered clouds, we set detection thresholds for LWP_{MW} and δTc for low, middle and high overcast cases. These thresholds must be established such that the layers are distinct. Thus, we account for the potential thickness of the clouds and the uncertainties in Tw and LWP_{MW}. Because Tw represents the cloud center and Tc corresponds more to cloud-top temperature, the two layers must be separated by more than half the cloud thickness. Low and midlevel mean cloud thicknesses of ~0.72 and 0.94 km, respectively, were derived from the island radiosonde data. The mean thickness for midlatitude high-level clouds from Wang and Rossow (1995) is ~2.5 km. Based on these thickness estimates, values of 3, 5, and 10 K are used to conservatively approximate the temperature differences between the cloud top and center for the three cloud categories. Because of the Tw uncertainties [*Lin et al*. 1997], 5 K more temperature differences are added to above values to separate different cloud layers. Thus, the δTc threshold between single and multilayered clouds is the sum of the half-thickness temperatures and 5K, or 8, 10, 15 K for low, middle, and high clouds, respectively. The LWP_{MW} threshold is selected to be 0.04 kg/m^2 to account for the LWP_{MW} uncertainties (~ 0.04 kg/m^2). Thus, all observations are defined to be multi-layered clouds, if LWP_{MW} > 0.04 kg/m^2 and δTc > 8, or 10, or 15 K for low, middle and high clouds, respectively.

Using these criteria, the cloud overlapping frequencies for the overcast low,

middle and high clouds are about 0%, 19% and 36%, respectively. The lack of multilayered clouds in the low-cloud cases is due to the uncertainties in the MW cloud temperature retrieval method and to the small range of possible temperatures for the low-cloud case. Although some studies find low clouds overlap other low clouds [e.g., *Wang and Rossow* 1995], the distance between the two layers is usually so small (< 1 km) that MW methods cannot separate the two cloud layers (Figure 8a). In overcast middle and high cloud cases, the frequencies of multi-layered clouds are lower than the global occurrence of multi-layered clouds [*Wang and Rossow* 1995], but comparable to the values (~30%) in a northeastern Pacific subtropical marine stratocumulus region area where ship observations were available [*Wang and Rossow* 1995]. Examination of the radiosonde-derived cloud layers over Santa Maria and Porto Santo show that midlevel clouds overlapped low clouds in approximately 30% of the samples. Only three high-level cloud cases were detected and, of these, two were above lower cloud decks. Few multilayered low cloud cases were determined. The greater frequency of midlevel overlapped cloud cases in the radiosonde data may be caused by using only the overcast midlevel cloud cases from the satellite data, to biased sampling over the islands, or to the sensitivity of multilayer determination to the applied thresholds. While sensitivity tests show that a 5-K change in the high-level thresholds will have little effect on the derived frequency of overlapped clouds, a similar change in midlevel threshold can change the frequency of overlap by ~10%, indicating that MVI method can more accurately detect systems with ice clouds over water clouds than those of multilayered water clouds. Lowering the LWP_{MW} threshold would tend to increase the number of overlapped clouds also. Given the uncertainties in cloud thickness and *Tw*, the selected thresholds seem to be quite reasonable and probably do not overestimate the overlap occurrence frequencies.

During ASTEX, an 8-mm Doppler radar was used to monitor cloud boundaries over the island of Porto Santo [*Uttal and Frisch* 1994]. The cloud boundaries were determined objectively with an automated method that can detect multi-layered cloud systems [*Uttal et al.* 1993]. To develop a comparable dataset, the radar boundaries during a given hour were examined for multi-layered clouds using height-difference thresholds equivalent to the δTc's applied to the MW data. Because it is difficult to distinguish clouds from ground clutter in the radar returns below 300 m [*Uttal and Frisch* 1994], only cloud boundaries above 300 m were considered. The radar data yield 0, 21, and 36% overlap for low, middle, and high cloud cases, respectively, for the period June 1 - 28, 1992. Although these data represent only a small area, they are very consistent with the IR-MW retrieval of multilayered clouds for the ASTEX domain.

A closer comparison is possible using only the paired SSM/I and Meteosat data in the 0.5° regions surrounding Porto Santo. Only those times are considered when the HBTM cloud cover is greater than 95% resulting in only 13 independent cases having SSM/I, Meteosat, and Porto Santo radar data. The HBTM-derived cloud heights for all of the regions surrounding the island were averaged for the low, middle, and high layers. A single mean cloud height was computed from the SSM/I retrievals. The radar returns corresponding to the satellite data were averaged in the following manner. The atmosphere was divided into 100-m thick layers. For each radar pulse, it is theoretically possible to have a return in each layer. The number of returns in each layer was determined for the 1-hour periods centered on the relevant Meteosat image times. Figure 9a shows the comparison for cases when the radar detected clouds within a given layer in at least 5% of the returns. Figures 9b and 9c depict the same comparison except that the radar returns within a given layer must occur in minimum of 50 and 95%, respectively, of the total pulses.

Most of the returns reveal only low-level clouds that are generally thin and broken. The radar-derived clouds disappear from many of the samples when the radar probability is increased to 95% (Figure 9c). Sample 2 shows a return only in the lowest layer. Because returns in this layer are assumed to be noise or ground clutter, no clouds were detected over the island in sample 2. Examination of the satellite imagery revealed that the island was clear while the surrounding ocean was generally overcast. The island cloud cover was totally low overcast for samples 10, 11, and 12. The agreement between the HBTM and the radar returns is very good for all of the single-layer cases with the HBTM heights close to the top altitudes observed by the radar. The SSM/I-retrieved heights are typically lower than the radar and HBTM for these thin/broken clouds as expected from the earlier discussion of the

uncertainties in the retrieval of *Tw* (also cf. *Lin et al*. [1997]). If 50% radar probability is used as reference, MVI cloud heights are within the cloud layers found by 8mm radar for most cases. For example, the MVI results are reasonably agree with radar observation the clouds in sample 12.

Multilayered clouds, as defined for the SSM/I data, are observed in only two of the cases, samples 1 and 9. Neither case was classified as middle or high overcast by the HBTM. The maximum altitudes from the HBTM are below the base of the highest layer detected by the radar suggesting that the high clouds are optically thin and overlap with the low stratus deck at ~2.6 km (Figure 9c) for sample 1. Although no clouds were observed by the radar near 4 km, both the SSM/I and HBTM place clouds at that altitude. This result may be due to the presence of liquid water in the lower levels of the thin high cloud, i.e. maybe there are some middle clouds nearby the island. If the high clouds are optically thin, the radiation received by the IR sensors would be a combination of emission from both the middle and high clouds producing equivalent blackbody temperatures between those corresponding to the middle and high clouds, as indicated by the altitude of the highest HBTM clouds compared to the base of the highest layer from the radar. Although the HBTM results for sample 9 also suggest thin cirrus overlying low stratus, there is no indication of high-level liquid water in the SSM/I retrieval. The SSM/I cloud height is the same as that determined for many of the single-layer cases. Although the ideal comparisons (overcast upper-level cloud with underlying liquid water cloud) are not available in this matched dataset, the results demonstrate that the SSM/I retrieval can determine cloud heights that are generally within about 1 ~ 2 km of the true liquid-water-cloud altitude and can detect low-level liquid water clouds below cirrus.

The detailed data in Figure 9 and the favorable statistical comparison of multilayer cloud frequencies for the ASTEX domain with those from Porto Santo for the entire period provide additional support to the conclusion that the present MVI method can separate cloud layers when high ice clouds overlap lower liquid water clouds as proposed by *Lin et al*. [1997]. A more precise estimate of the accuracy of this method for determining the presence of multilayered clouds will require much additional study using both satellite and ground/aircraft based observations.

e. Effective particle radius

From equation (1), we can estimate r_e using LWP_{MW} and LWP_{VIS} determined for all clouds except overcast high clouds. The histograms of r_e (Figure 10) are similar for all three cloud categories with means between 12 and 13 μm and standard deviations around 10 μm. The relatively large standard deviations of r_e and the spread in the histograms indicate that effective droplet radius is highly variable in this marine stratocumulus domain. The r_e modes range from 6 to 8 μm, values considerably smaller than the corresponding means. Median values of r_e vary from 9.7 to 10.5 μm for all clouds. The frequencies of $r_e > 16$ μm vary from 28 to 33% compared to a range of 19 to 24% for $r_e > 20$ μm. The latter criterion is associated with theoretical estimates of drizzling clouds, while the former is based on an empirical study based on ASTEX in situ aircraft data [*Gerber* 1996].

These estimates are subject to uncertainties arising from several sources. Thin ice clouds overlying the lower clouds will produce reflectances greater or less than those for the low cloud alone depending on the satellite-sun-cloud angles. Such errors will induce either over- or underestimates of r_e and optical depth. The negative values of r_e are due to the negative values of LWP_{MW} discussed earlier. Their inclusion in the histograms and statistics offsets some overestimates of *LWP* that may give rise to some of the extremely large effective radii. Obviously, they are physically unrealistic and unacceptable in any evaluation of cloud particle sizes. Their impact can be eliminated by only using data having LWP_{MW} above a minimum threshold as in the multilayer retrieval analysis. Any errors in the Meteosat VIS calibration would tend to bias the results. The non-plane parallel nature of real clouds will cause some errors in the optical depth retrievals especially for the high solar zenith angles in these observations and for the scenes containing broken clouds. Some scale effects, discussed below, may also impact the droplet size retrievals. Spatial and temporal mismatches will influence the retrievals. Because of their relatively large size, the SSM/I footprints may lie only partially in a given region, so that LWP_{MW} may include clouds from adjacent regions and may miss some of the clouds within the region. The mismatch between the region

and the SSM/I footprint will induce a random error in the derived droplet sizes because the LWP_{VIS} and LWP_{MW} will be representative of slightly different mixes of clouds. The net result of this effect will be a broadening or larger standard deviation of the droplet-size range. A similar effect occurs because of the time differences between the two satellite views.

The mean value of r_e ~12.5 μm is less than the zonal mean derived from July 1987 NOAA-9 data by *Han et al.* [1994] for ocean regions between 20°N and 40°N. For the ASTEX domain, however, the average *Han et al.* [1994] droplet radii vary from 8 to 15 μm and appear to be less than the zonal mean. Those data were taken during the afternoon, while the present results were derived from early morning and late afternoon measurements. The relatively large number of small particles revealed in Figure 10 are probably due to the frequent influx of continental aerosols into the eastern part of the ASTEX domain [e.g., *Randall et al.* 1996]. *Han et al.* [1994] also found smaller values of r_e over the eastern part of the domain in the July 1987 data. Despite the differences in the time periods covered by the *Han et al.* [1994] analysis and the present study, the agreement between the two results is quite good.

Some of the differences are due to the physical limitations of the retrievals. The NOAA-9 analysis lacks sensitivity to particle size for $r_e > 32$ μm, while the droplets extend up to 40 μm in this study. Another cause for discrepancies in the results may be differences in the sensitivities of the MVI and *Han et al.* [1994] methods to the vertical distribution of cloud droplets. The latter and similar multispectral reflectance techniques are generally most responsive to the upper portions of thick clouds and may not account for the droplet sizes in the lower portions of clouds because of the absorption characteristics of water droplets at near-infrared wavelengths. The MW retrieval tends to sense all of the liquid water in cloud forcing the retrieval of VIS optical depth and effective radius to account for all of the droplets. In the typical non-drizzling stratus cloud, the droplets increase in size with altitude. Although the effective radius is generally larger in drizzling clouds, the largest droplets will be located lower in the cloud and below cloud base. The drizzle droplets will be much larger than the average cloud droplet causing a significant increase in r_e when heavy drizzle occurs [*Gerber* 1996]. Thus, the reflectance methods may tend to overestimate r_e in non-drizzling clouds and underestimate r_e in drizzling clouds. These different sensitivities may help explain why the frequency distributions in Figure 10 are broader and have smaller mode values than those found by *Han et al.* [1994]. Other reasons for the relatively large spread in the Figure 10 distributions were discussed above.

Zuidema and Hartmann [1995] and *Greenwald et al.* [1995] used matched Earth Radiation Budget Experiment (ERBE) broadband shortwave albedos and SSM/I data taken over 2.5° regions to derive r_e for low overcast marine clouds. Their results produced mean values between 10.1 and 11.1 μm with standard deviations approximately half of the values found here. The differences between their results and those in Figure 10 may be due to several factors. One of the most important reasons may be the differences in sampling times and locations. Another may be the scales. The grid area used here is only 1/25 that of the ERBE-SSM/I results. Small-scale variability is more easily detected with smaller pixels and will likely be averaged out over 250 km. Thus, larger standard deviations are expected for the ASTEX dataset. The mean effective droplet size may also be influenced by scale because of the nonlinear dependencies of reflectance or albedo on optical depth and droplet size. Simple averaging of the reflectance over large areas will yield different values of optical depth and r_e than those derived from smaller areas before averaging. For example, if we use the mean values of LWP_{MW} and LWP_{VIS} from Figure 7 in equation (1), we obtain r_e about 11 μm a value within the range found in the studies using the 2.5°-region data. However, it is almost 2 μm smaller than the average of the individual retrievals.

The differences between the means and modes in Figure 10 may be due to the frequent occurrence of drizzle during ASTEX and to the dominance of maritime air over a significant part of the ASTEX domain. Using aircraft in situ measurements, *Gerber* [1996] determined that larger droplets and drizzle were quite frequent during ASTEX. He found that for light drizzle (drizzle LWC < 0.01 gm^{-3}), the effective radius is not significantly influenced by the presence of a few drizzle droplets. At larger drizzle LWC's, the influence becomes important. Heavy drizzle (drizzle LWC > 0.01 gm^{-3}) was often found to occur whenever $r_e > 16$ μm. If that is the case, then heavy drizzle was occurring in about 30% of the clouds sampled here compared to about 29%

in the 25°N-40°N ocean zone found in the *Han et al*. [1994]. The flights comprising the *Gerber* [1996] datasets detected heavy drizzle in only 15% of the samples. In contrast, the median effective radius measured in the *Gerber* [1996] data is almost identical to that found here. It is not known how well the aircraft measurements represent ASTEX as a whole. Therefore, we cannot conclude whether the percentage of drizzling clouds based on the *Gerber* [1996] criterion is overestimated by the MVI retrievals. It is encouraging, however, that the frequency of drizzling clouds is essentially the same as that from the *Han et al*. [1994] retrievals. Despite some of the differences noted above, the results determined with the MVI method are generally consistent with both aircraft and other satellite-remote sensing values of r_e for marine stratocumulus clouds and can be used to study the gross microphysical properties of the ASTEX clouds, especially when averages over large areas or time periods are considered.

The derived values of Tc, LWP_{MW}, and r_e were correlated to determine if a relationship exists between these variables. Figure 11 shows the scatter plots of LWP_{MW} and Tc for low and midlevel overcast and all cloudy atmospheres, respectively, without the negative values. A slightly negative correlation coefficient (R = -0.25) was found between Tc and LWP_{MW} for low clouds (Figure 11a), while a stronger positive correlation (R = 0.37) resulted for midlevel clouds (Figure 11b). The negative correlation is similar to that found by *Zuidema and Hartmann* [1995] for low stratus clouds. The opposite behavior for the middle clouds is surprising, but it may be due to thin cirrus over low stratus causing lower IR cloud temperatures. In Figure 11b, a large cluster of points extends from 280K, 0.1 kg m^{-2} to larger values of LWP_{MW} and slightly colder temperatures, as expected for colder thicker clouds. The remainder of points show small values of LWP_{MW} at temperatures that range from 275 to 260K. This more or less random distribution of small LWP_{MW} at the colder temperatures is similar to that observed for high clouds in Figure 3c. Thus, if the cold portion of the data (Tc < 275K) is excluded, a negative correlation (R = -0.23) is found between the midlevel cloud temperature and LWP_{MW}. No correlation exists between LWP_{MW} and Tc for overcast high clouds (not shown). The correlation for all cloudy atmospheric cases (Figure 11c) is relatively strong (R = -0.26) and similar to that for overcast low clouds. Most of these cloudy atmospheres comprise broken and scattered low clouds.

Despite the large spread in each plot in Figure 12, effective radius appears to be more correlated with LWP_{MW} than with Tc (cf. Figure 13). Removal of the colder scenes (Tc < 275K) in the midlevel cloud case increases R to 0.41. The positive correlations suggest that the droplets are generally larger in the thicker clouds which would be consistent with a greater probability of drizzle in those clouds. *Zuidema and Hartmann* [1995] also found an indication that r_e increases with LWP. The correlations between r_e and Tc shown in Figure 13 produced $-0.04 < R < 0.16$ indicating little possibility of a relationship between the two parameters. Removal of the colder midlevel clouds (Figure 13b) decreases R to 0.08. These results indicate that cloud height may be less important in determining the sizes of cloud liquid water particles than the number densities of cloud condensation nucleus, aerosols and relative humidity within clouds [*Houze* 1993; *Hobbs* 1993].

5. Concluding Remarks

In this study, the microwave-visible-infrared technique used the HBTM analyses of Meteosat data to determine cloud optical depth and cloud-top temperature. The technique, however, can easily be used with other VIS-IR methods [e.g., *Rossow et al*. 1991; *Minnis et al*. 1995] and applied to data taken from combinations of any satellite instruments that include channels similar to those used here. The current results were based on data taken in relatively ideal conditions: low, often single-layered, marine stratus with an overlying dry atmosphere. Other regions such as the tropics will present a greater challenge because of a moister atmosphere, more vertically developed clouds, and frequent overlapping of various cloud types. Thus, additional testing and refinement of the MVI method is warranted. A more exact matching of the SSM/I fields of view with the geostationary satellite data will likely decrease the variance of the LWP and r_e retrievals. It will also permit correction of the microwave retrieval for partial cloudiness in the field of view.

This paper has demonstrated the capabilities of the MVI method for deriving a variety of cloud properties including the detection

of liquid water clouds below thick cirrus. Typical VIS-IR methods must assume that the cloud effective droplet radius is constant and that the cloud exists in only one layer. Recently developed, multispectral solar-infrared techniques have the capability to detect low clouds below optically thin high clouds and can yield estimates of cloud particle size. However, low clouds cannot be detected if the upper level cloud is optically thick. This new MVI technique shows promise for improving the determination of cloud overlap for optically thick cases over ocean. Separation of the upper and lower layers would improve estimates of the cloud water and atmospheric radiation budget because the total contribution in terms of both radiation and mass could be computed for the liquid and ice phase. With knowledge of the lower-layer *LWP* and temperature, it should be possible to determine the upper-layer cloud temperature and *IWP* more accurately based on the IR and VIS radiances and radiative transfer calculations. The independent determination of liquid cloud temperature will also permit the identification of water in or below what may appear to be only an ice cloud to other multispectral methods. Because low and middle level clouds are basically warm and cloud thicknesses are generally unknown, the MVI method usually cannot separate single-layered from multi-layered water clouds. More studies are needed to improve the multilayer determinations for warm clouds.

Retrievals of cloud droplet size using the MVI method are generally consistent with the multispectral solar-infrared results and in situ aircraft data indicating that the two techniques may be used interchangeably. If additional research confirms this conclusion, then more complete monitoring of daytime, marine effective cloud droplet sizes will be feasible by routinely applying both methods to available satellite data. Diurnal cycles of effective radius, conversion of polluted to clean air masses, the movement of drizzling cloud systems, and other marine cloud properties could be quantified more easily and accurately than current observational methods allow. With additional improvements and validation for clouds in other climate regimes, the MVI technique will be extremely valuable for enhancing our understanding of oceanic clouds.

Acknowledgments

This research is supported by the NASA Radiation Processes Program and the Earth Observing System (EOS)/Interdisciplinary Program, NASA/Office of Mission to Planet Earth through the Clouds and the Earth's Radiant Energy System (CERES) Project. One of our authors (BL) thanks NASA for support under contract NAS1-19656. Some of the satellite data analyses were supported by the Office of Naval Research through R. F. Abbey under Grant USN-N0001491IMP24011. The DMSP data were provided by the Distributed Active Archive Center at the NASA Marshall Space Flight Center in Huntsville, Alabama. F. Wentz of Remote Sensing Systems in Santa Rosa, California supplied the algorithms for reducing SSM/I antenna temperatures. The 1992 Meteosat data were purchased from the European Space Agency with the assistance of Genevieve Seze of the Laboratoire Meteorologie Dynamique in Paris, France.

References

Albrecht, B. A., Boundary layer cloud studies in support of ASTEX. *Marine Meteorology Abstract Book FY 1995*, Office of Naval Research Report 32296-6, January, pp. 1-3, 1996. [Available from ONR Code 322, 880 N. Quincy St., Arlington, VA 22217-5660]

Baum, B. A., R. F. Arduini, B. A. Wielicki, P. Minnis, and S. C. Tsay, Multilevel cloud retrieval using multispectral HIRS and AVHRR data: nighttime oceanic analysis, *J. Geophys. Res*. **99**, 5499-5514, 1994.

Charlock, T., F. Rose, T. Alberta, G. L. Smith, D. Rutan, N. Manalo-Smith, P. Minnis, and B. Wielicki, Cloud profiling radar requirements: Perspective from retrievals of the surface and atmospheric radiation budget and studies of atmospheric energetics. Utility and Feasibility of a Cloud Profiling Radar, WCRP-84, IGPO Publication Series No. 10, January, B10-B21, 1994.

Gerber, H., Microphysics of marine stratocumulus clouds with two drizzle modes, *J. Atmos. Sci*., **53**, 1649-1662, 1996.

Goodberlet, M. A., C. T. Swift, and J. C. Wilkerson, Ocean surface wind speed measurements of Special Sensor Microwave/Imager (SSM/I), *IEEE*, **GE-28**, 832-828, 1990.

Greenwald, T. J., G. L. Stephens, T. H. Vonder Haar, and D. L. Jackson, A physical retrieval of cloud liquid water over the global oceans using SSM/I observations, *J. Geophys. Res*., **98**, 18471-18488, 1993.

Greenwald, T. J., G. L. Stephens, S. A. Christopher, and T. H. Vonder Haar, Observations of global characteristics and regional radiative effects of marine cloud liquid water. *J. Climate*, **8**, 2928-2946, 1995.

Gupta, S. K., W. L. Darnell, and A. C. Wilber, A parameterization for surface longwave radiation from satellite data: Recent improvements, *J. Appl. Meteor*., **31**, 1361-1367, 1992.

Hahn, C. J., S. G. Warren, J. Gordon, R. M. Chervin, and R. Jenne, Atlas of simultaneous occurrence of different cloud types over ocean. NCAR Tech. Note TN-201 + STR , 212 pp., 1982.

Hahn, C. J., S. G. Warren, J. Gordon, R. M. Chervin, and R. Jenne, Atlas of simultaneous occurrence of different cloud types over land. NCAR Tech. Note TN-241 + STR , 211 pp., 1984.

Han, Q., W. B. Rossow, and A. A. Lacis, Nearly global survey of effective droplet radii in liquid water clouds using ISCCP data, *J. Climate*, **7**, 465-497, 1994.

Heymsfield, A. J., Microphysical structures of stratiform and cirrus clouds, in *Aerosol-Cloud-Climate Interactions*, edited by P.V. Hobbs, Academic, San Diego, Calif., 1993.

Hobbs, P. V., *Aerosol-Cloud-Climate Interactions*, edited, Academic, San Diego, Calif., 1993.

Houze, R. A., Jr., *Cloud Dynamics*, Academic, San Diego, Calif., 1993.

Lin, B., and W. B. Rossow, Observations of cloud liquid water path over oceans: Optical and microwave remote sensing methods, *J. Geophys. Res*., **99**, 20907-20927, 1994.

Lin, B., and W. B. Rossow, Seasonal variation of liquid and ice water path in non-precipitating clouds over oceans , *J. Climate*, **9**, 2890-2902, 1996.

Lin, B., and W. B. Rossow, Precipitation water path and rainfall rate estimates over oceans using Special Sensor Microwave Imager and International Satellite Cloud Climatology Project data, *J. Geophys. Res*., **102**, 9359-9374, 1997.

Lin, B., B. A. Wielicki, P. Minnis, and W. B. Rossow, Estimation of water cloud properties from satellite microwave, infrared and visible measurements in oceanic environments. I: Microwave brightness temperature simulations, submitted to *J. Geophys. Res*., 1997.

Liu, G., and J. A. Curry, Determination of characteristic features of cloud liquid water from satellite microwave measurements, *J. Geophys. Res*., **98**, 5069-5092, 1993.

Luo, G., X. Lin, and J. A. Coakley, Jr., 1994: 11-μm emissivities and droplet radii for marine stratocumulus, *J. Geophys. Res.*, **99**, 3685-3698.

Minnis, P., E. F. Harrison, and G. G. Gibson, Cloud cover over the equatorial eastern Pacific derived from July 1983 International Satellite Cloud Climatology Project data using a hybrid bispectral threshold method. *J. Geophys. Rev*. **92**, 4051-4073, 1987.

Minnis, P., P. W. Heck D. F. Young, C. W. Fairall and J. B. Snider, Stratocumulus cloud properties derived from simultaneous satellite and island-based instrumentation during FIRE, *J. Appl. Meteorol*., **31**, 317-339, 1992.

Minnis, P., P. W. Heck, and D. F. Young, Inference of cirrus cloud properties using satellite-observed visible and infrared radiances, Part II: Verification of theoretical cirrus radiative properties, *J. Atmos. Sci.*, **50**, 1305-1322, 1993.

Minnis, P., W. L. Smith, D. P. Garber, J. K. Ayers, and D. R. Doelling, Cloud properties derived from GOES-7 for spring 1994 ARM intensive observing period using version 1.0.0 of ARM satellite data analysis program, NASA reference publication 1366, 1995.

Nakajima, T., and M. D. King, Determination of the optical thickness and effective particle radius of clouds from reflected solar radiation measurements, Part I: Theory, *J. Atmos. Sci*., **47**, 1878-1893, 1990.

Nakajima, T., M. D. King, and J. D. Spinhirne, Determination of the optical thickness and effective particle radius of clouds from reflected solar radiation measurements, Part II: Marine stratocumulus observations, *J. Atmos. Sci*., **48**, 728-750, 1991.

Pandey, C. P., E. G. Njoku, and J. W. Waters, Inference of cloud temperature and thickness by microwave radiometry from space, *J. Clim. Appl. Meteor*., **22**, 1894-1898, 1983.

Petty, G. W., On the response of the special sensor microwave/imager to the marine environment--Implications for atmospheric parameter retrievals, Ph.D. dissertation, Dept. of Atmos. Sci., Univ. of Washington, Seattle, 1990.

Poore, K., J. Wang, and W. B. Rossow, Cloud layer thicknesses from a combination of

surface and upper-air observations, *J. Climate*, **8**, 550-568, 1995.

Randall, D. A., B. Albrecht, S. Cox, D. Johnson, P. Minnis, W. Rossow, and D. O'C. Starr, *On FIRE at ten*. Adv. Geophys., **38**, 37-177, 1996.

Rossow, W. B., L. C. Garder, P. J. Lu, and A. W. Walker, International Satellite Cloud Climatology Project (ISCCP) documentation of cloud data, WMO/TD No. 266 (Revised), World Meteorological Organization, Geneva, 77 pp., 1991.

Schluessel, P., and W. J. Emery, Atmospheric water vapor over oceans from SSM/I measurements, *Int. J. Remote Sensing*, **11**, 753-766, 1990.

Snider, J. B., D. A. Hazen, A. J. Francavilla, W. B. Madsen, and M. D. Jacobson, Island- and ship-based radiometric measurements of water vapor, cloud liquid, and solar flux during the Atlantic Stratocumulus Transition Experiment (ASTEX). NOAA Technical Memorandum (in press), 1996.

Stephens, G.L., The parameterization of radiation for numerical weather prediction and climate models, *Mon. Wea. Rev*., **112**, 826-867, 1984.

Syrett, W. J., Low-level temperature and moisture structure from ASTEX radiosondes: 1-28 June 1992, Pennsylvania State University Report, 200 pp., 1993 [Available from Department of Meteorology, Pennsylvania State University, University Park, PA 16802].

Tian, L., and J. A. Curry, Cloud overlap statistics, *J. Geophys. Res*., **94**, 9925-9935, 1989.

Twomey, S., Atmospheric aerosols, Developments in atmospheric sciences, Vol. 7, Elsevier, 302pp, 1977.

Uttal, T., L. I. Church, B. E. Martner, and J. S. Gibson, CLDSTATS: A cloud boundary detection algorithm for vertically pointing radar data. NOAA TM ERL WPL-233, July, 28 pp., 1993.

Uttal, T. and A. S. Frisch, Cloud boundaries during ASTEX. *Proc. AMS 8th Conf. Atmospheric Radiation*, Nashville, TN, Jan. 23-28, 259-261, 1994.

Wang, J., and W. B. Rossow, Determination of cloud vertical structure from upper-air observations, *J. Appl. Meteor*., **34**, 2243-2258, 1995.

Warren, S.G., C. J. Hahn, and J. London, Simultaneous occurrence of different cloud types, *J. Climate Appl. Meteor*., **24**, 658-667, 1985.

Warren, S.G., C. J. Hahn, J. London, R. M. Chervin, and R. L. Jenne, Global distribution of total cloud cover and cloud type amounts over ocean, NCAR Tech. Note NCAR/TN-317+STR, 42 pp., plus 170 maps, 1988.

Wentz, F. J., User's Manual, SSM/I Antenna Temperature Tapes, Revision 2. *RSS Tech. Report 032588*, Remote Sensing Systems, Santa Rosa, CA, 34 pp., 1993. [Available from the author at 1101 College Ave., Suite 220, Santa Rosa, CA 95404]

Wielicki, B. A., J. T. Suttles, A. J. Heymsfield, R. M. Welch, J. D. Spinhirne, M.-L. C. Wu, D. O'C. Starr, L. Parker, and R. F. Arduini, The 27-28 October 1986 FIRE IFO cirrus case study: Comparison of radiative transfer theory with observations by satellite and aircraft, *Mon. Wea. Rev*., **118**, 2356-2376, 1990.

Wielicki, B. A., R. D. Cess, M. D. King, D. A. Randall, and E. F. Harrison, Mission to planet earth: Role of clouds and radiation in climate, *Bull. Am. Meteorol. Soc*., **76**, 2125-2153, 1995.

Young, D. F., P. Minnis, K. Katsaros, A. Dybbroe, and J. Miletta, Comparison of techniques for deriving water-cloud microphysical properties from multiple satellite data. *Proc. 11th Intl. Conf. on Clouds and Precip.*, Montreal, Canada, Aug. 17-22, 1053-1056, 1992.

Zuidema, P. and D. L. Hartmann, Satellite determination of stratus cloud microphysical properties. *J. Climate*, **8**, 1638-1657, 1995.

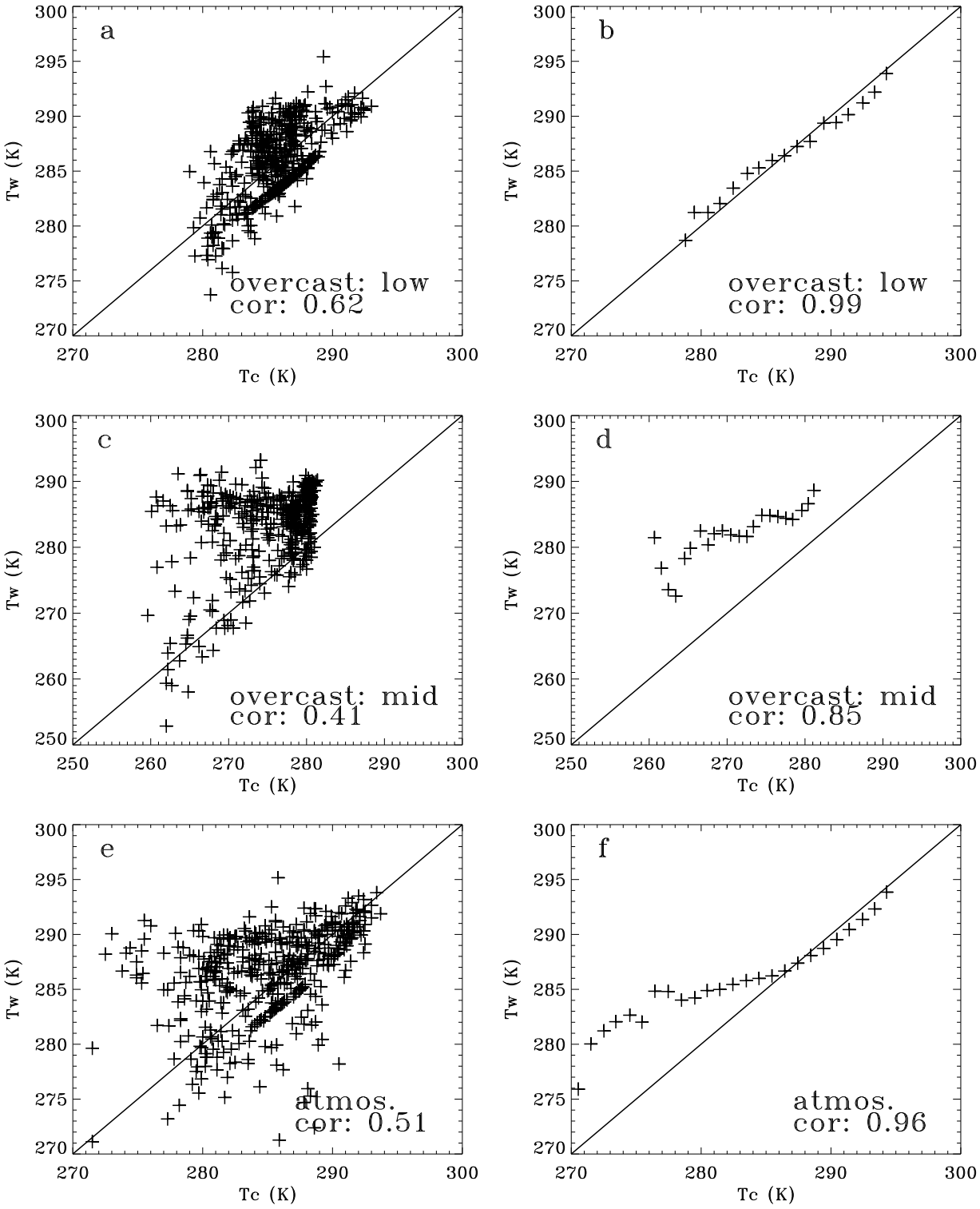

Figure 1. Scatterplot of coincident microwave and infrared cloud temperatures. Left panels (a,c,e) are from 500 random samples. Right panels (b,d,f) are averages of all data for 1-K intervals.

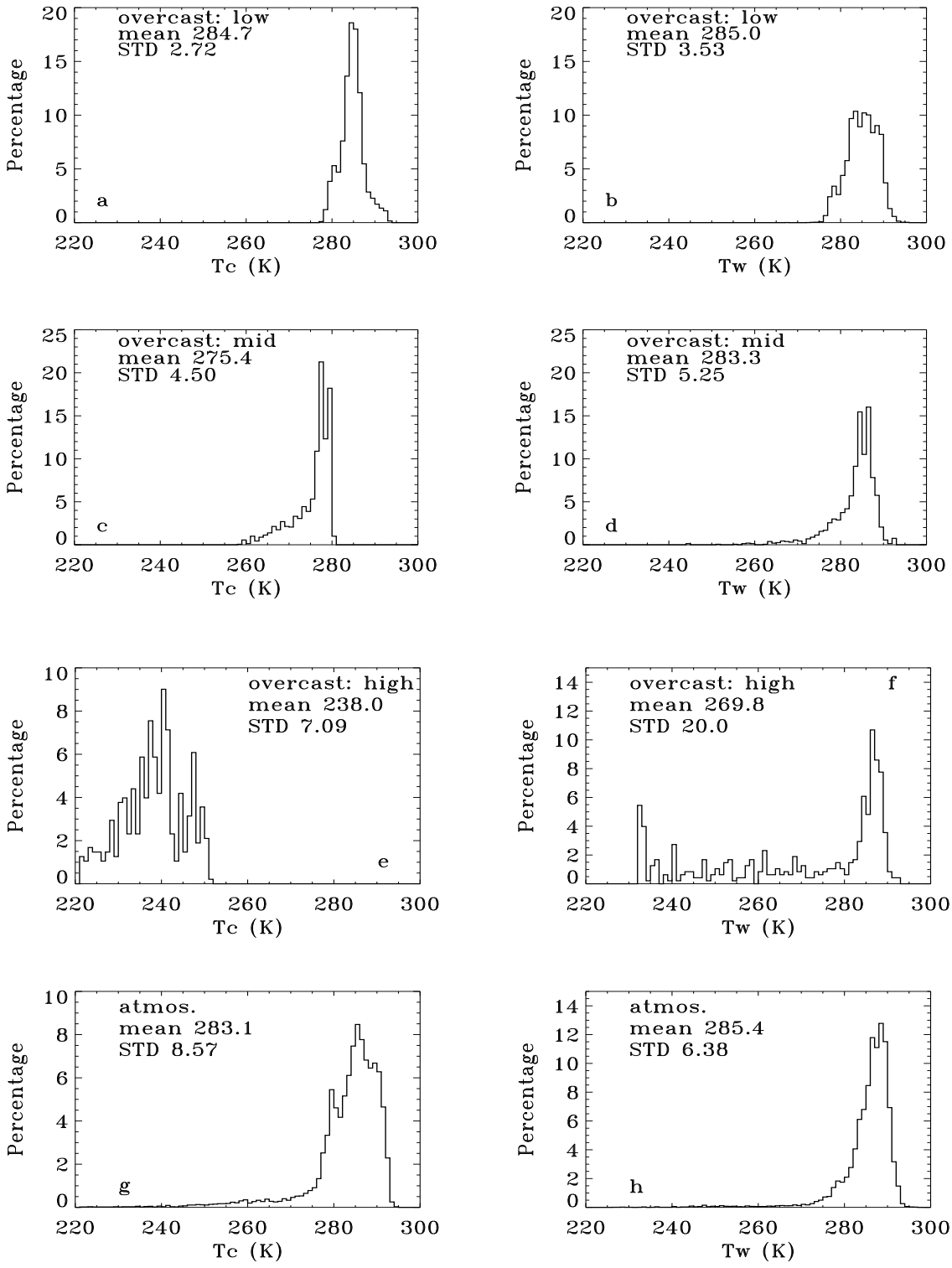

Figure 2. Frequency distributions of cloud temperature from HBTM and microwave method for overcast low (a, b), middle (c, d), high (e, f), and for total cloud conditions (g, h).

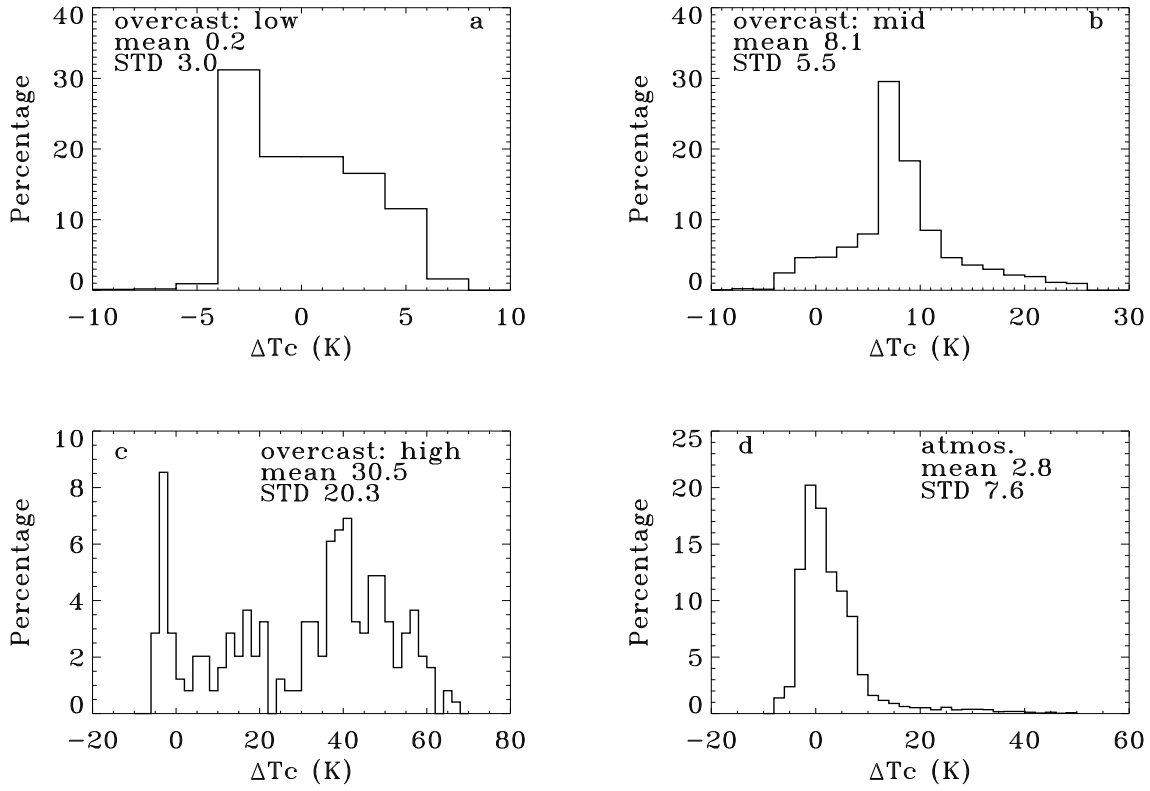

Figure 3. Frequency distributions of differences between MW and IR cloud temperatures for overcast a) low, b) middle, c) high, and d) all other clouds.

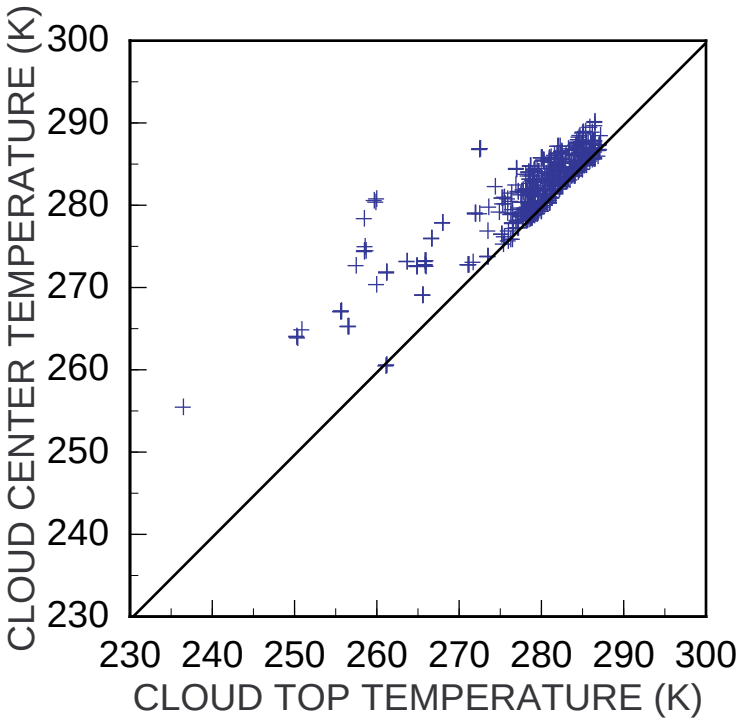

a) Mean center cloud temperature computed for all layers

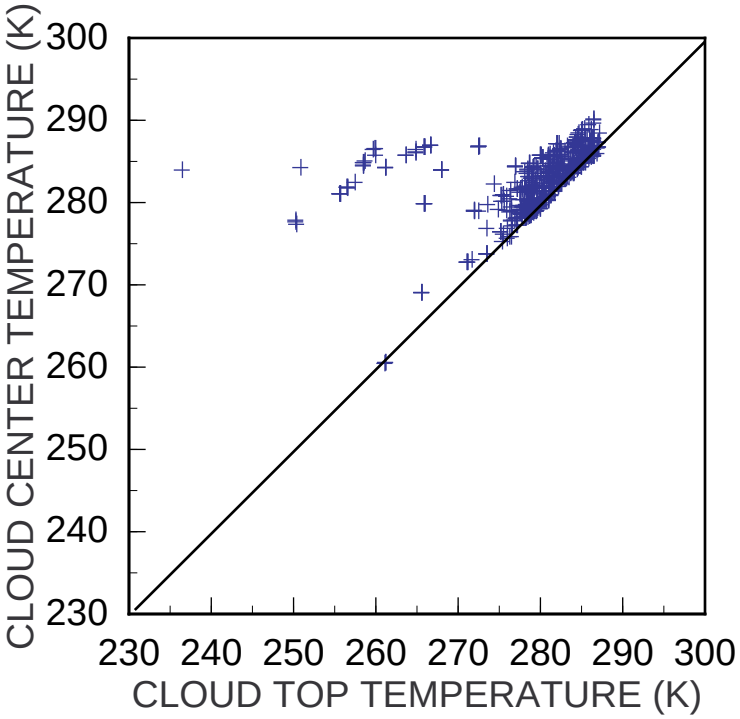

b) Mean center cloud temperature computed for all layers except for top layer with $Tc < 270$K.

Figure 4. Comparison of cloud-top and cloud-center temperatures based on radiosonde data from Santa Maria and Porto Santo Islands, 1 - 28 June 1992.

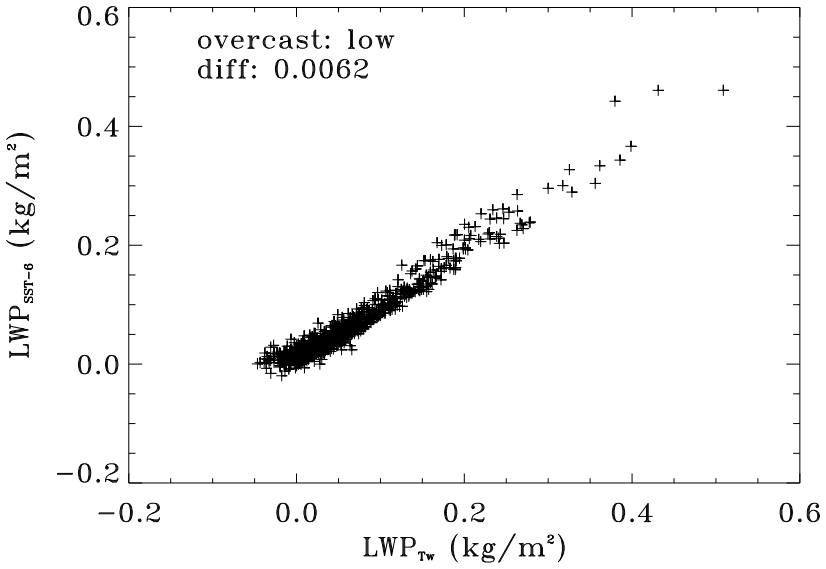

Figure 5. Comparison of *LWPMW* from the current and *Greenwald et al.* [1993] methods.

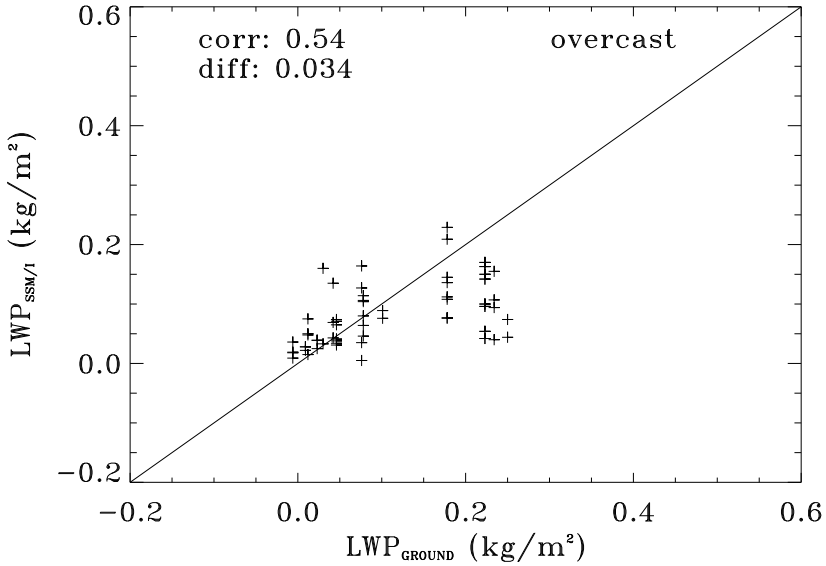

Figure 6. Comparison of *LWPMW* from the current method and ground-based observations.

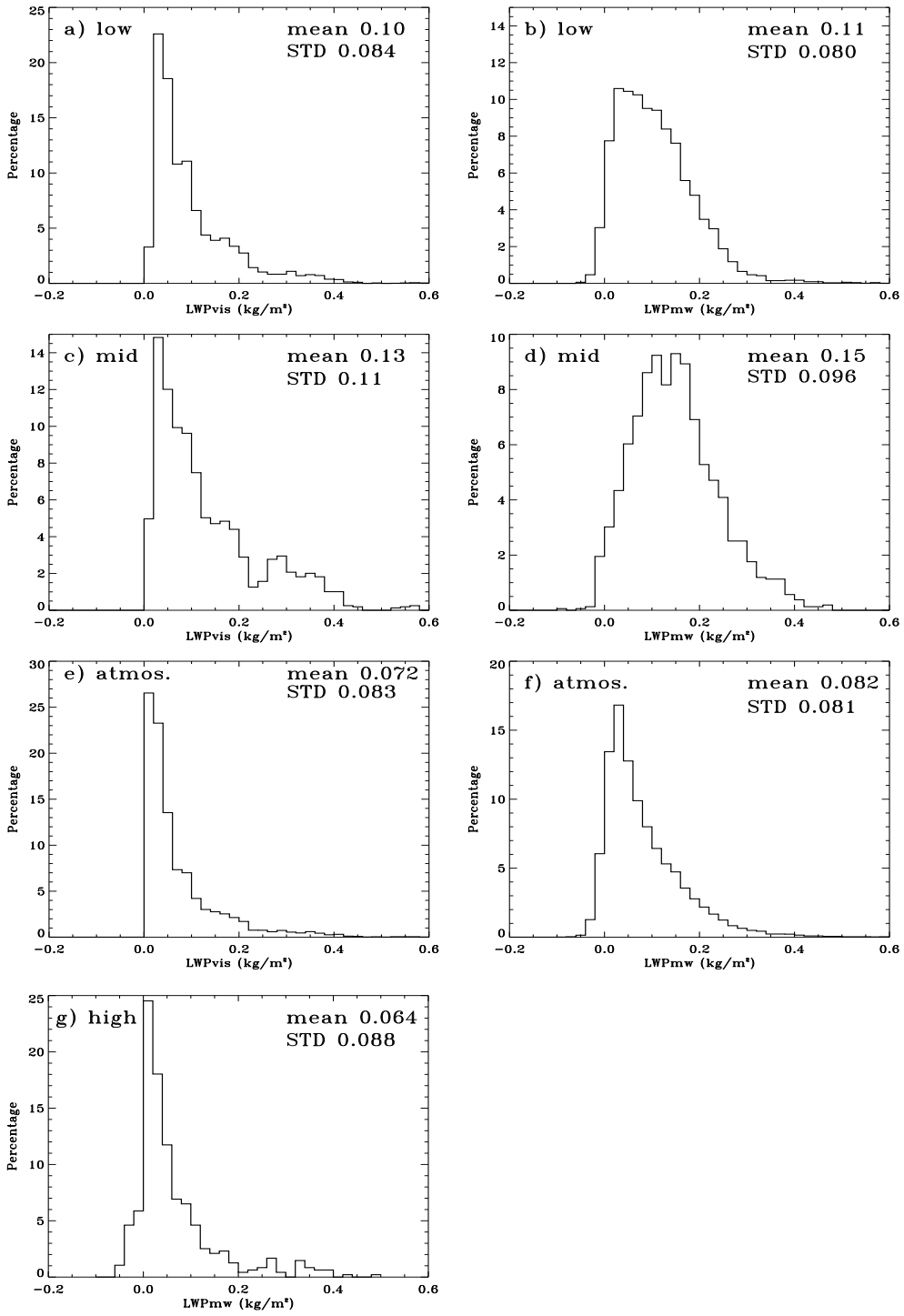

Figure 7. Histograms of cloud liquid water path from HBTM (a,c,e) and microwave method (b,d,f). Only microwave-derived *LWP* is given for high clouds (g).

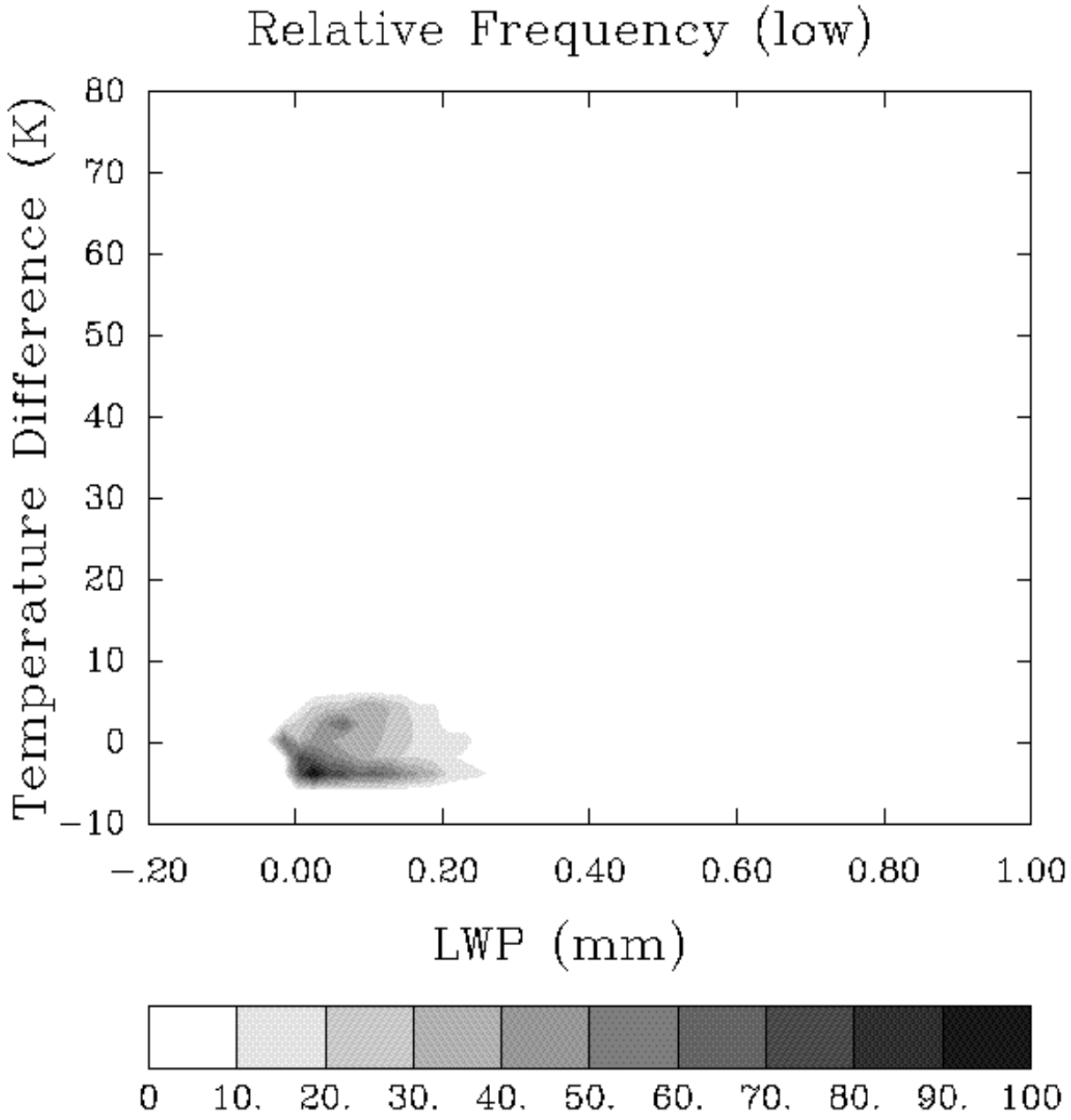

Figure 8a. Relative frequencies of LWP_{MW} and δTc for overcast low clouds.

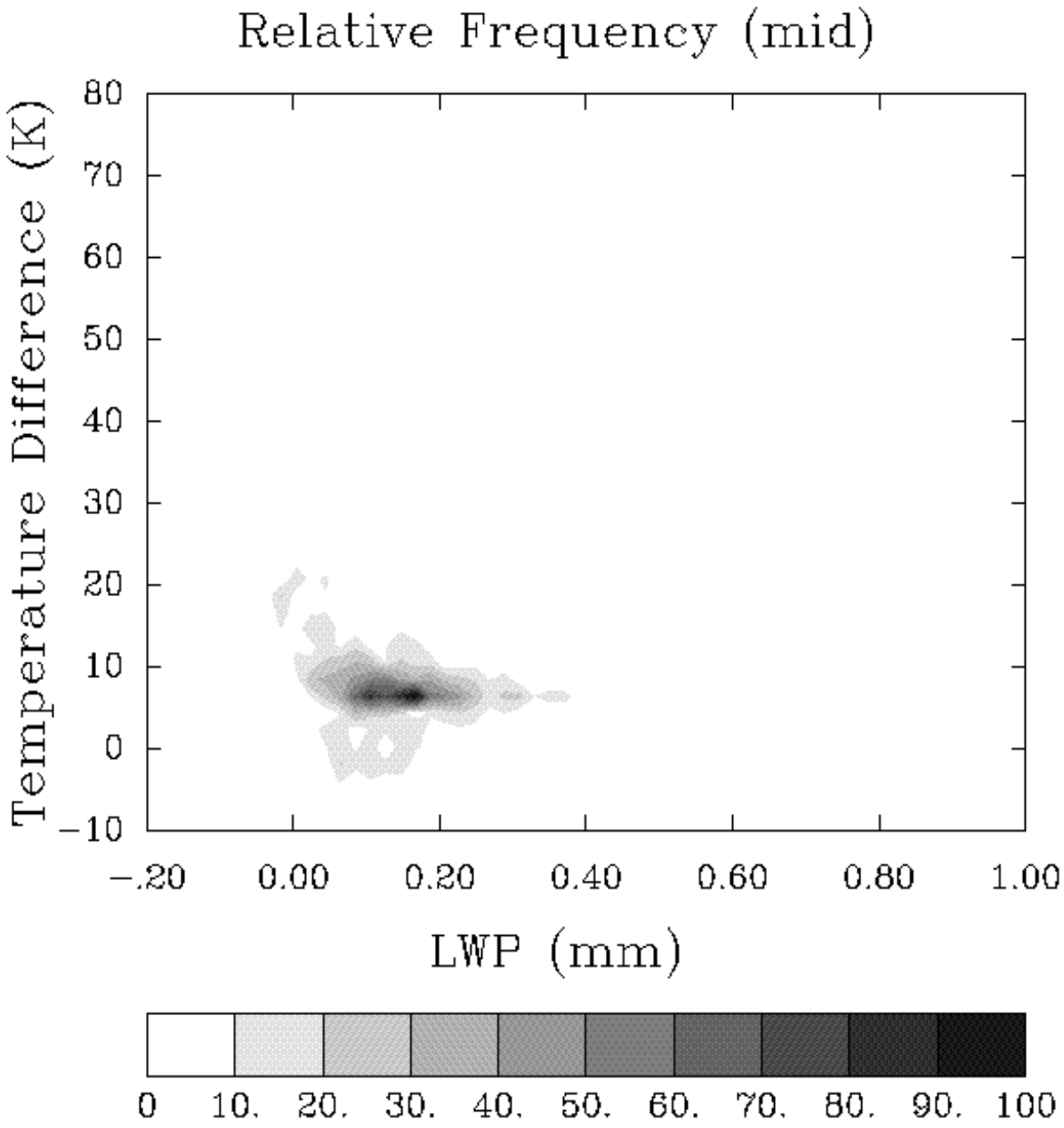

Figure 8b. Relative frequencies of LWP_{MW} and δTc for overcast midlevel clouds.

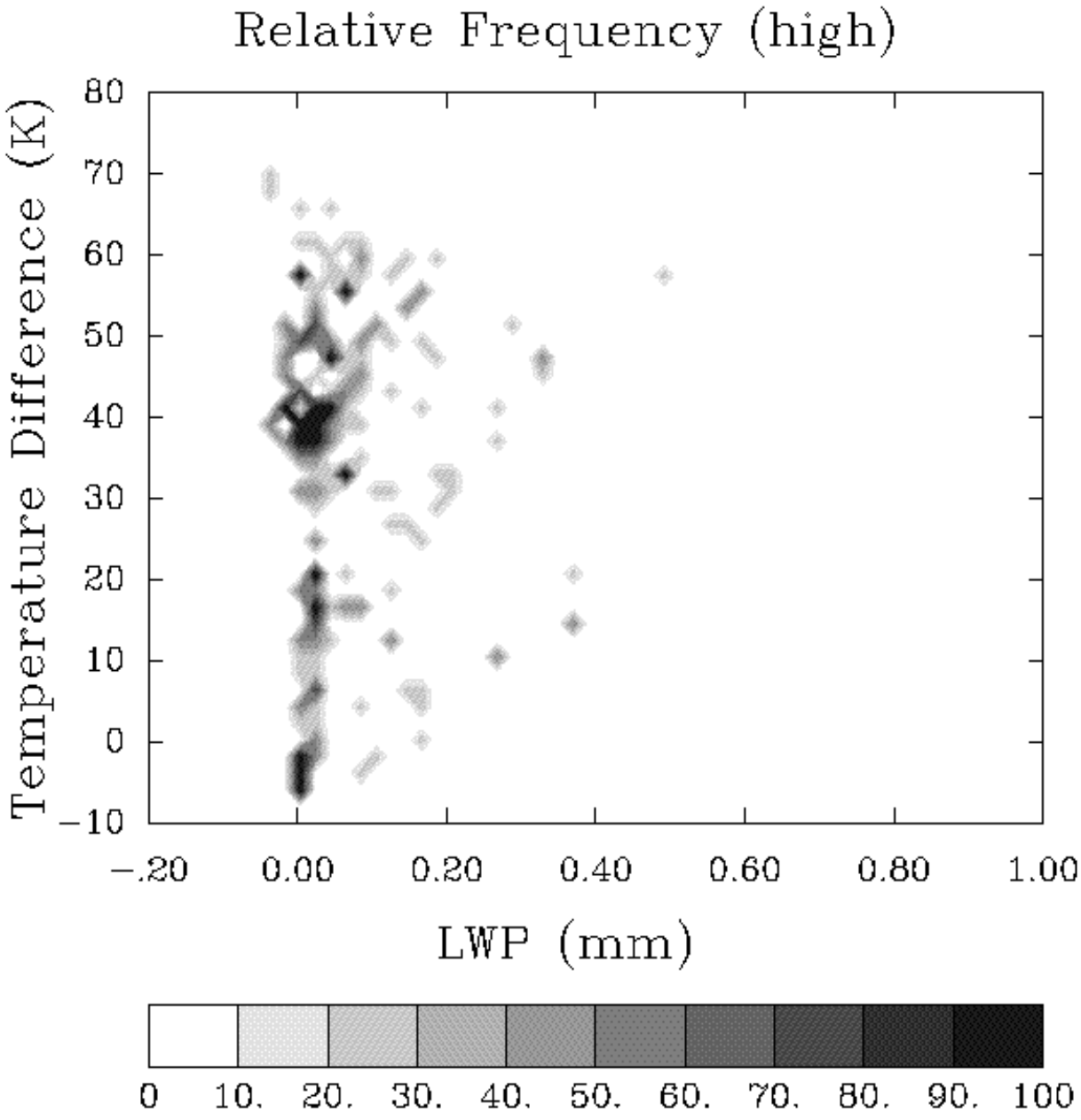

Figure 8c. Relative frequencies of LWP_{MW} and δTc for overcast high clouds.

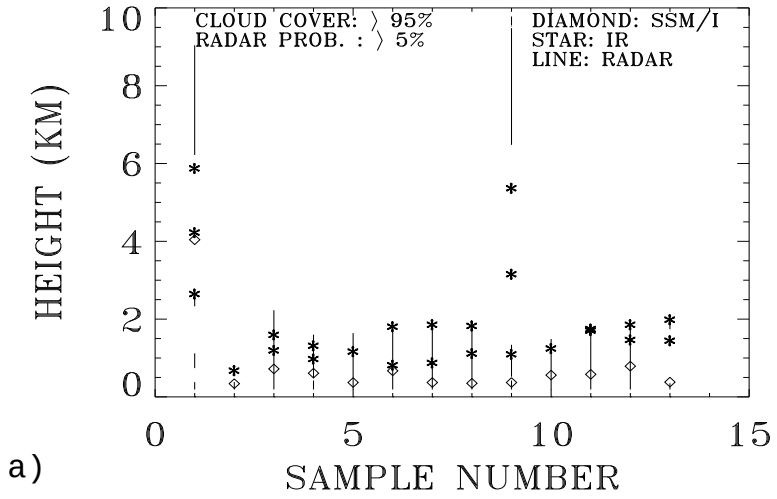

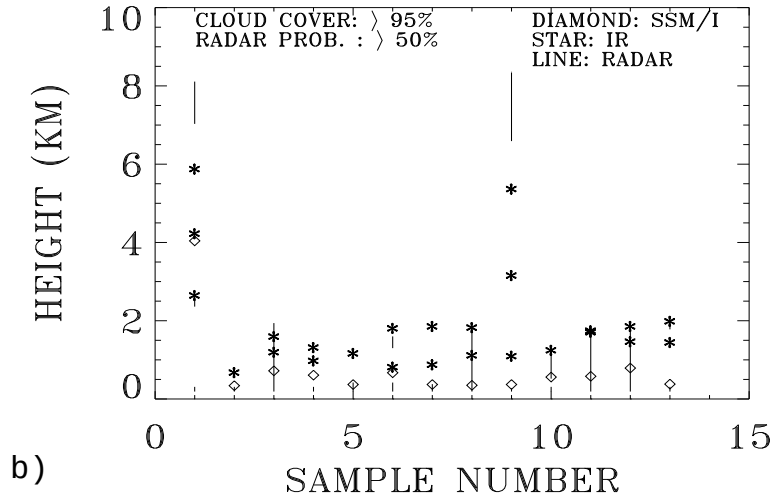

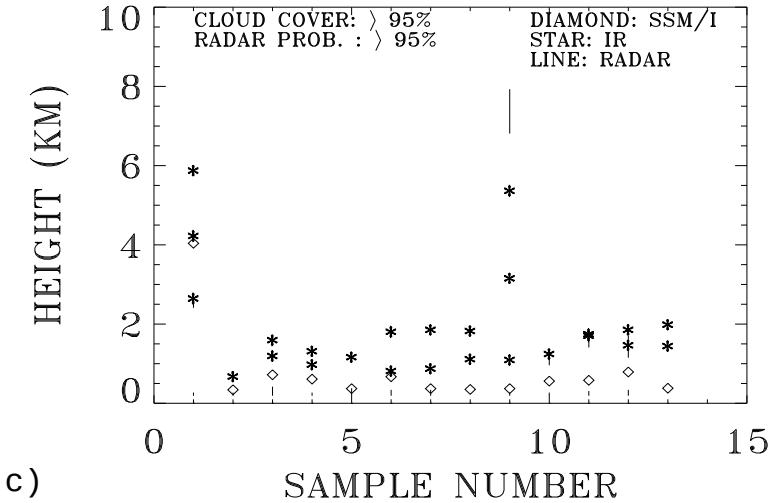

Figure 9. Comparison of satellite IR (star), MW (diamond), and ground-based radar (solid line) cloud heights for more than 95% cloud cover. Figures a), b), and c) show the layers in which, at least, 5%, 50%, and 95%, respectively, of the radar returns have detected clouds.

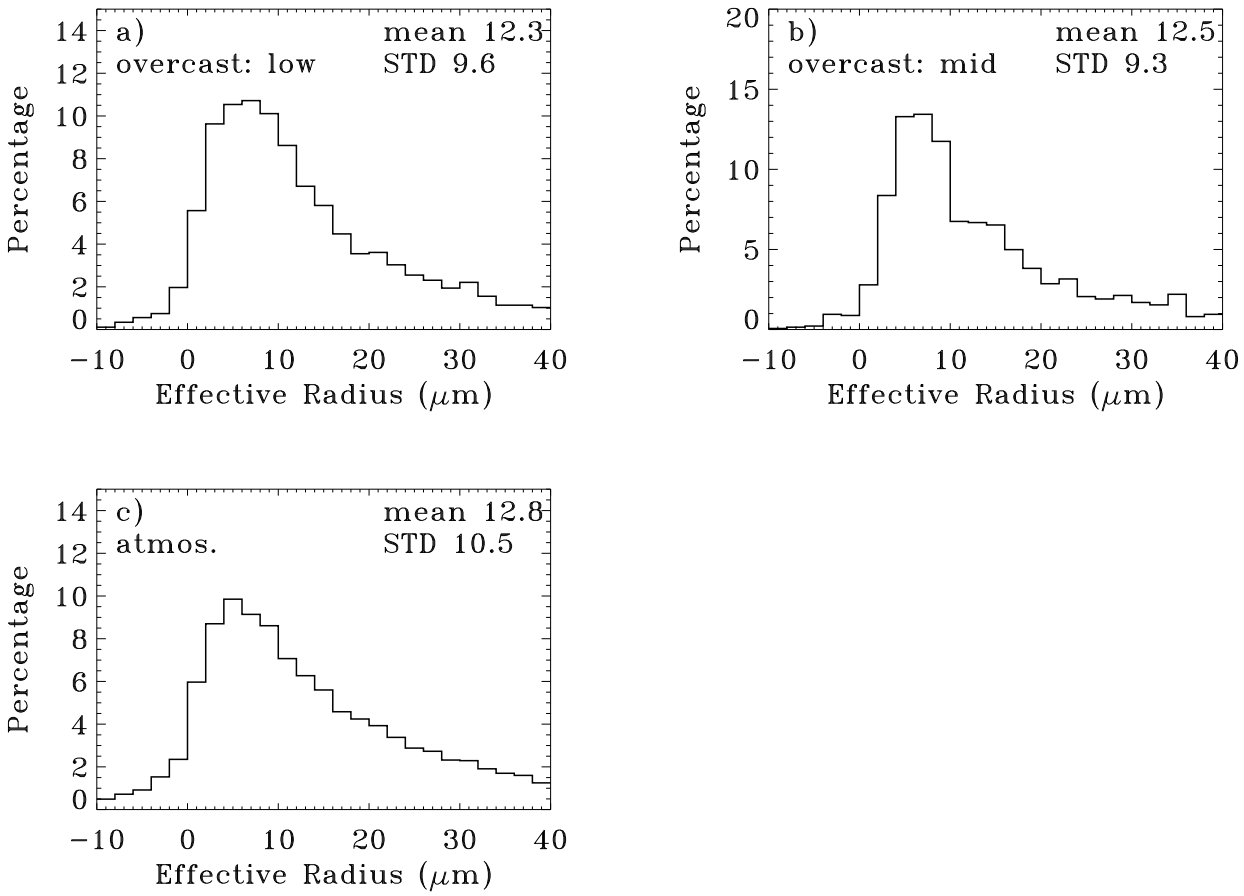

Figure 10. Histograms of cloud effective droplet radius for a)low overcast, b) middle clouds, and for c) all clouds.

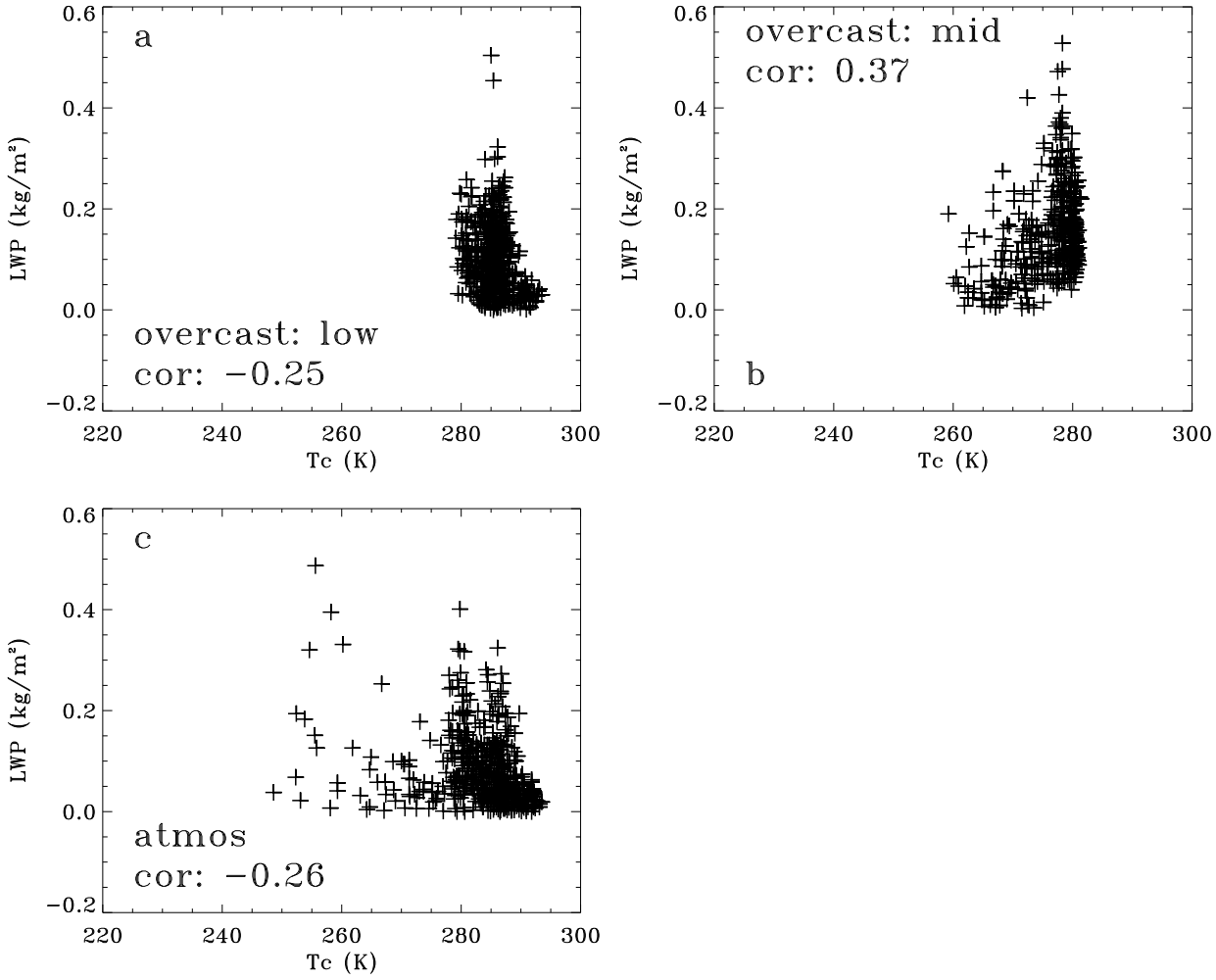

Figure 11. Scatterplots of *LWPMW* and *Tc* for overcast a) low and b) middle clouds and for c) all cloudy conditions.

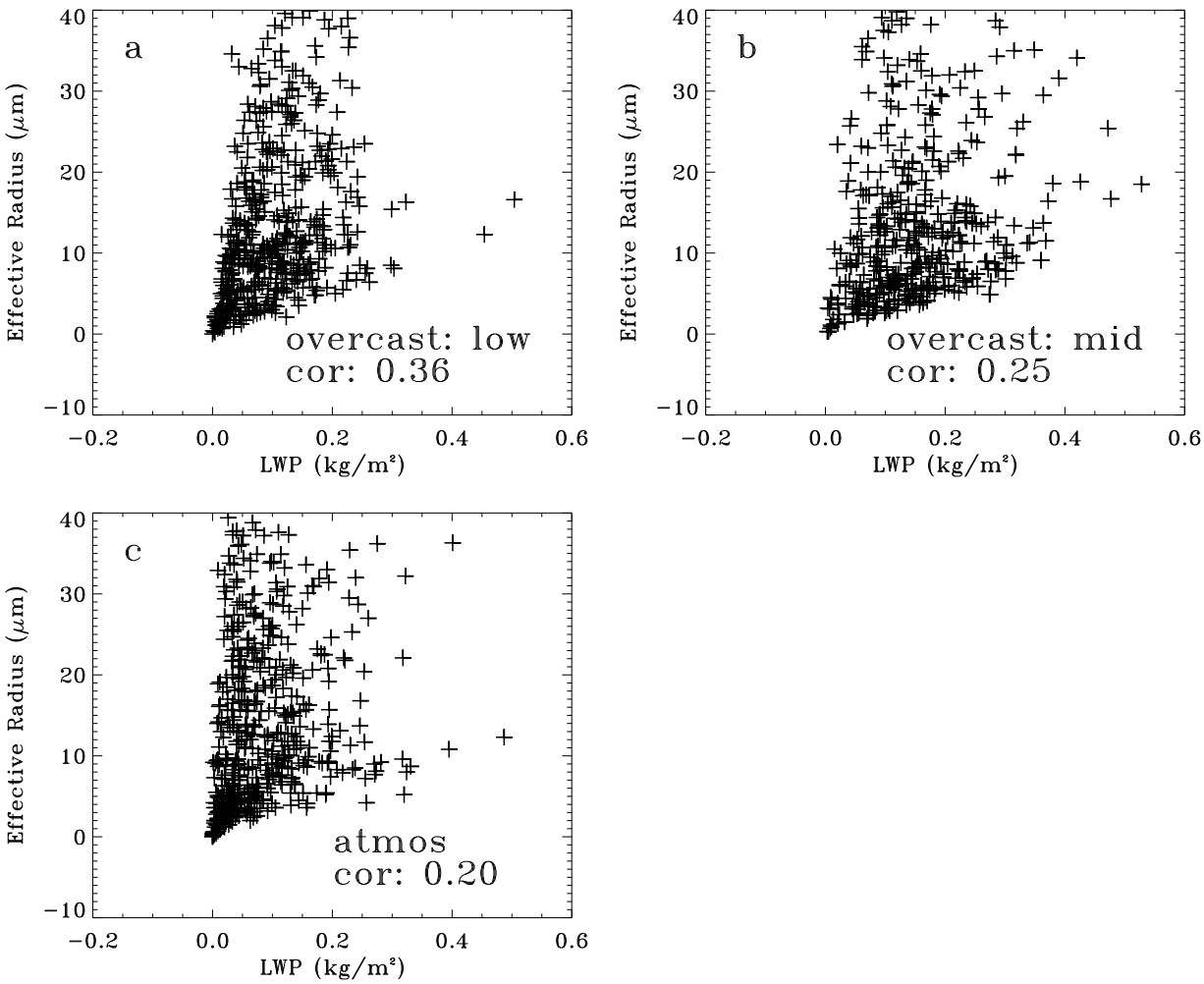

Figure 12. Same as Figure 11, but for r_e and LWP_{MW}.

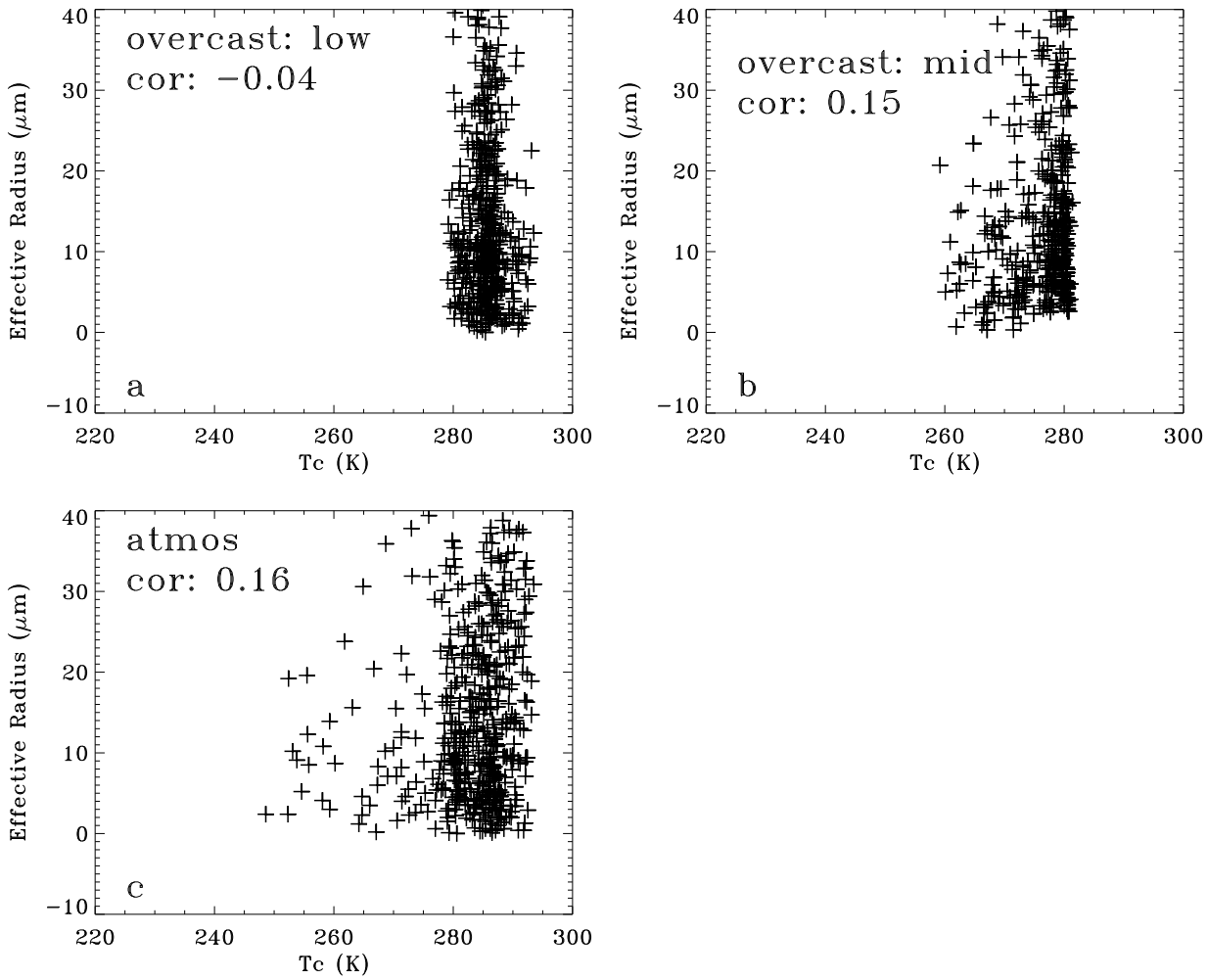

Figure 13. Same as Figure 11, but for *re* and *Tc*.